The Pennsylvania State University

The Graduate School

Department of Electrical Engineering

CHARACTERIZATION OF THE WAVE-LARS POLARIZATION LIDAR TRANSMITTER AND RECEIVER

A Thesis in

Electrical Engineering

by

George R. Evanisko

Submitted in Partial Fulfillment
of the Requirements
for the Degree of

Master of Science

December 1994

We approve the thesis of George R. Evanisko

Date of Signature

Charles R. Philbrick Professor of Electrical Engineering Thesis Advisor	
Timothy J. Kane Prof. Electrical Engineering	
Daniel B. Lysak Jr. Research Associate	
Larry C. Burton Professor of Electrical Engineering Head of the Department of Electrical Engineering	

Abstract

The characterization of the lidar transmitter and receiver portion of the WAVE-LARS (Water, Aerosol, Vapor Experiment-Lidar and Radar Sounder) research instrument is presented. The WAVE-LARS instrument objectives are to deduce aerosol size distributions, determine cloud thermodynamic phases, provide information on aerosol distribution, and describe optical propagation conditions in the lower atmosphere. These goals are accomplished by using a scanning three wavelength Rayleigh/Raman lidar which also determines the depolarization ratio.

The characterization of the lidar transmitter and receiver is critical in understanding the system performance. The transmitter stability, polarization, efficiency, and energy are examined to determine how each will effect the return backscattered signal. The receiver optical setup has been modeled to determine where each wavelength enters completely into the telescope's field of view. The receiver elements, including the telescope, polarization divider box, and optical fibers, are reviewed and the instrument efficiency is discussed. Preliminary data taken with the system is presented in the final chapter. In addition, the plans for future work with the system are discussed.

Table of Contents

List of Figures

List of Tables

Acknowledgements

First, I would like to thank God.

I would like to thank Dr. C. R. Philbrick for being my advisor and guiding me during my assistantship and my M.S. thesis.

In addition, I would like to thank Dr. Lysak and Dr. Kane for serving on my committee and assisting me with my thesis.

Finally, and most importantly, I would like to thank all my co-workers who aided me during my research, Mike O'Brien, Bob Smith, Jim Anuskewicz, Glenn Pancoast, Brian Mathason, Paul Haris, Jim Yurack, Tim Stevens, Subha Maruvada, Sumati Rajan, Steve McKinley, Tom Petach, and Stephen Sprague.

Chapter 1

Introduction

Everyone has experienced a cooling effect on the skin caused by clouds blocking the sunlight. Some people may know that it is warmer at night if it is overcast compared to a clear sky. Few people understand specular reflections off of ice crystals in cirrus clouds produce haloes. The common link is the optical properties of clouds, but a hidden relationship lies in the clouds impact on global radiative heat transfer. At any given instance, clouds cover approximately 40 to 50 percent of the Earth. No doubt then, there is a valid reason to study clouds and how they affect the climate.

Clouds vary in shape, size, thickness, altitude, particle make-up, etc. How do these factors affect the heating or cooling of the Earth? Does a cloud reflect more shortwave solar radiation or longwave Earth radiation? Does the radiation get absorbed, extincted, scattered and re-emitted towards Earth or space? How can lidar measurements be best used to describe optical propagation characteristics such as extinction and visibility? Finding the answers to these questions and similar questions about clouds and aerosols are important in determining the role both play in the radiative transfer in the lower atmosphere.

Several instruments are capable of investigating clouds and aerosols. They include weather balloons, radar, satellites, aircraft and lidar. All of these instruments either interact and disturb the medium or do not provide suitable spatial and temporal resolution, except one, that one is lidar (LIght Detection And Ranging). A lidar instrument aims short (10^{-9} sec), intense laser pulses into the atmosphere and collects the backscattered photons in range gated bins. The data from the range bins can provide information on temperature, size, shape, and

molecular concentration of scatterers in the atmosphere. A lidar's resolution elements can be as small as 7.5 meters and can be observed in near real time (the data acquisition system is the limiting factor).

In order to study clouds and aerosols, we have developed the WAVE-LARS scanning lidar/radar research instrument. WAVE-LARS is an acronym for Water, Aerosol, Vapor Experiment-Lidar And Radar Sounder. For the remainder of this thesis, only the lidar portion of the instrument will be discussed and will be referred to as LARS. The first chapter will describe a lidar instrument, scattering principles and techniques, and the lidar equation. In addition it will outline the goals of the LARS system.

1.1 Basic Lidar Instruments

A lidar system usually consists of five basic subsystems: a transmitter, receiver, detector, data acquisition, and safety system. The transmitter consists of the laser, energy monitor, beam expander, and beam steering mirrors. When the laser is triggered, the laser beam is steered by mirrors along an optical path into the atmosphere. A percentage (dependent on the scattering medium and range) of the outgoing photons are backscattered toward the receiver. The receiver is usually a telescope used to collect the photons. The photons are then directed through an optical system on the back of the telescope and into the detector section. The detector section uses lenses, thermally stabilized filters, beamsplitters and photomultiplier tubes or semiconductor detectors to split and detect the received wavelengths. The detectors are chosen for their spectral response, quantum efficiency, active area, dark noise, etc. and these characteristics are matched to the particular wavelengths being

used to study the atmosphere. A data acquisition section is connected to the detectors, in order to process and display the analog signal of the detectors. Finally, a set of safety devices are used to prevent injury due to high voltages or eye damage due to the intense laser pulses.

1.2 Scattering Principles

There are three scattering theories that are based on an isotropic, single particulate scattering situation, which are relevant to the LARS lidar: molecular (Rayleigh) scattering, particle (Mie) scattering, and molecular vibrational (Raman) scattering. The first two, Rayleigh and Mie scattering, are elastic scattering processes in which the frequency of the scattered light is equal to the incident laser frequency. (Rayleigh scattering also includes inelastic rotational Raman lines, because during Rayleigh's era, the equipment did not have a precise spectral resolution to separate the Raman lines.) Raman scattering is an inelastic scattering process that results in a frequency shift, of the incident laser frequency, that is unique to the type of molecule being illuminated.

The determination of whether the molecular or particle scattering theory applies depends on the wavelength of the laser compared to the size of the scatterer. Rayleigh scattering theory is applied when the scattering particle is much smaller than the incident wavelength. Since the LARS system uses three laser wavelengths closely spaced, 1064, 532, and 355 nm, Rayleigh theory applies to scatterers that are usually molecules or atoms. This is why the term Rayleigh scattering is frequently applied to molecular scattering. Small aerosols can also be considered in Rayleigh scattering theory, when they are small compared to the wavelength. For the 94 GHz LARS radar, the particles and droplets that make up

clouds are also considered Rayleigh scatterers when they are small compared to the wavelength of the radar, 3.2 mm. Because the troposphere and stratosphere contain many aerosol particles much larger than the incident laser wavelengths, pure molecular scattering does not become the dominant process until altitudes greater than 25 kilometers, or sometimes greater altitudes following volcanic eruptions.

The Rayleigh backscattering cross section is,

$$\sigma_{\pi}^{R} = \frac{\pi^2 (n^2 - 1)^2}{N^2 \lambda^4} \quad , \qquad \textbf{(1.1)}$$

where n is the refractive index of the scatterer, N is the number density of the scatterers, and λ is the incident wavelength (Measures, 1992). As can be seen, Rayleigh scattering has a λ^{-4} dependence and will exhibit a 81 times larger backscatter at 354.7 compared to 1064.1 nm. As an example, at sea level using a wavelength of 532 nm, a refractive index of 1.000293 for air, and a number density of 2.69×10^{19} molecules cm^{-3} (Loschmidt's number at STP), the backscatter cross section is equal to 5.85×10^{-28} cm^2 sr^{-1}.

Mie scattering is applied when a spherical scattering particle is comparable or much larger than the incident laser wavelength. With reference to the LARS lidar, Mie scattering is considered to be particulate scattering. The largest rain particles to the smallest aerosols in the atmosphere, can be considered in Mie scattering theory. The general equation for the Mie backscatter cross section is complicated (see Measurers, Chapter 2 for the actual equation) and is dependent on ka, n and θ, where ka is the scattering size parameter, n is the refractive index and θ is the scattering angle. The particle scattering cross section shows that

several large size aerosols can swamp the molecular backscatter return. Mie theory shows a λ^{-4} dependence, as would be expected, when the scattering particle becomes much smaller than the incident wavelength (reduces to Rayleigh theory).

Raman scattering is an inelastic scattering process. As an incident photon strikes a molecule, the photon raises the molecule to a virtual level. If the molecule then relaxes to an energy level different from the initial level, the resulting scattered frequency is shifted from the incident frequency by an amount unique to that molecule. A lower scattered frequency, longer wavelength, indicates the molecule has gained energy (Stokes line) while a higher scattered frequency indicates the molecule has lost energy (anti-Stokes line). The anti-Stokes vibrational lines of simple molecules are not excited at normal atmospheric temperatures because of the large energy spacing of the vibrational energy states. The Raman shift can be due to rotational or vibrational states of the molecule. The rotational Raman shift can result in frequency shifts between 10's and 100's cm^{-1}, while the vibrational Raman shift can result in frequency shifts between 100's and 1000's cm^{-1} of the incident frequency. A comparison of backscatter cross sections for the three processes are shown in Figure 1.

1.3 The Lidar Equation

The lidar equation is used to estimate the number of backscattered photons collected by the lidar system. There is a distinctive lidar equation used for each of the different lidar techniques, but all of the equations are related back to the basic lidar equation. This basic lidar equation, for elastic and inelastic scattering, is given below:

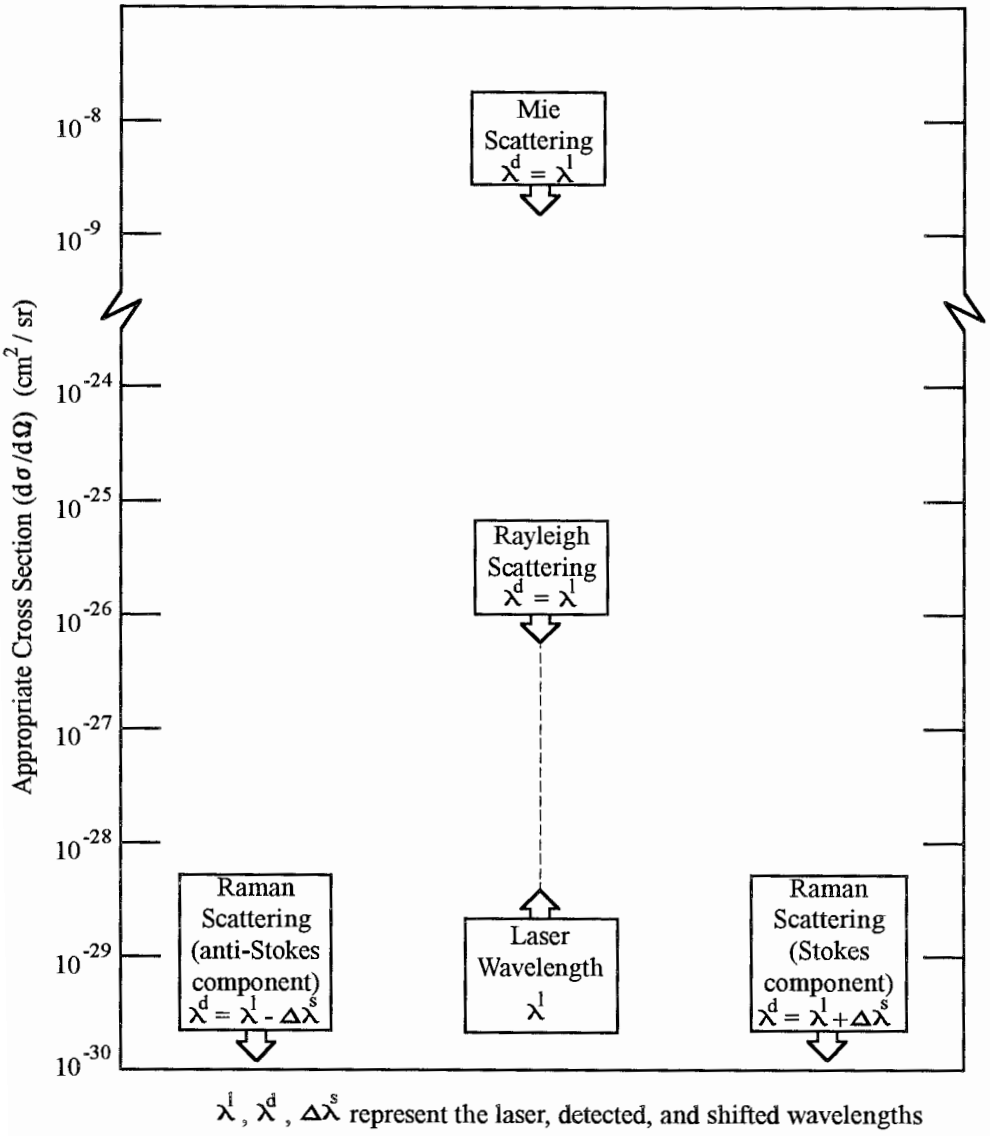

Figure 1.1. Comparison of backscatter cross sections relevant to LARS (Measures, 1992)

$$N(R) = \frac{E_T}{hc/\lambda_T} \times T(\lambda_T, R)T(\lambda_S, R) \times \frac{\sigma(\lambda_T, \lambda_S)n(R)\Delta R}{4\pi} \times \frac{\xi(R)A_o}{R^2} \times \xi_{eff}(\lambda_S) \quad \textbf{(1.2)}$$

(1) (2) (3) (4) (5) (6)

where,

(1) received number of photons from range R

(2) number of photons transmitted

(3) the integrated atmospheric transmission from the ground to range R of the transmitted and scattered wavelengths

(4) probability in range R of scattering

(5) probability of collecting photons from range R

(6) total optical efficiency of the receiver and detector at the scattered wavelength

and the parameters,

N(R) = number of photons returning from range R

E_T = the transmitted energy

h = Planck's constant

c = the speed of light

λ_T = the transmitted wavelength

$T(\lambda_T, R)$ = the integrated atmospheric transmission from the ground to range R of the transmitted wavelength

$T(\lambda_S, R)$ = the integrated atmospheric transmission from the ground to range

R of the scattered wavelength

$\sigma(\lambda_T, \lambda_S)$ = the total cross section for the scattered wavelength due to the transmitted wavelength

$n(R)$ = the atmospheric number density from range R

ΔR = the resolution or integration range

$\xi(R)$ = the geometric overlap factor of the telescope to the laser

A_o = the receiving telescope area

R = the range or distance from the receiver

$\xi_{eff}(\lambda_S)$ = the total optical efficiency of the receiver and detector at the scattered wavelength.

1.4 The Depolarization Ratio

The discussion on scattering (section 1.2) dealt with an ideal isotropic, single particle scattering situation. Most of the time however a visible lidar return signal from the lower atmosphere will include contributions from anisotropic scatterers and sometimes multiple scattering conditions. In order to investigate these situations, the depolarization ratio can be measured by lidar. The depolarization ratio is a measurement of the loss in polarization of the initially polarized laser beam. The basic definition is,

$$\delta_p \equiv \frac{P_\perp}{P_\parallel} \quad , \tag{1.3}$$

where $P_\perp$ is the power returned in the perpendicular direction and $P_\parallel$ is the power returned in the parallel direction with respect to the incident linearly polarized laser light. There are two

scattering processes which cause the change in the polarization of the scattered beam; anisotropic (irregularly shaped) particles and multiple scattering.

Anisotropic particles are particles that exhibit different properties along different axes. Several examples of these particles include: snow, hail, ice crystals, graupel, irregularly shaped particles (dust), etc. Because the particles are not spheres, upon being irradiated, the reflections and refractions from outside and inside the particle result in a change in polarization of the incident laser. In these cases the dipole field scattering, which preserves the polarization, is not found to occur. Since there are different basic shapes for each of the anisotropic particles, each shape will result in a distinct range of depolarization. For a cloud consisting of ice crystals, a depolarization of approximately 50% is common, while graupel is around 70% and a pure water droplet cloud is around 5% (Sassen, 1991). Even air has a depolarization ratio around 4% due to the anisotropy of the electric dipole field of the molecules (Measures, 1992).

Multiple scattering is a condition where more than one scattering interaction occurs in a medium before the photon is collected by the receiver. When the scatterers are closely spaced in a region, the illuminating beam can be scattered more than one time. With a visible lidar, scanning any medium having particles larger than haze particles is considered likely to produce multiple scattering. Since the radiation is interacting with multiple particles, the final description of the scattering becomes very difficult, if not impossible to solve. The depolarization ratio provides a way to detect the presence and extent of multiple scattering mediums.

As the lidar beam starts to penetrate a layer where multiple scattering exists, the

depolarization ratio starts increasing. The rate of increase of the ratio due to multiple scattering can be a result of several factors including field of view of the telescope, laser divergence, and cloud water particle concentration.

Since there are two principle causes for a depolarization of the laser beam, it may be difficult to determine whether multiple scattering events or anisotropic particles are causing the depolarization. Careful inspection of the data should provide the answer as to the cause. If the depolarization ratio starts at 5% upon entering a cloud and slowly increases, then the cloud is assumed to contain water droplets and the further increase is due to multiple scattering. If the ratio is 50% upon entering the cloud and slowly increases, then the cloud is assumed to contain ice crystals and multiple scattering. If there is a sudden jump in the depolarization ratio in a cloud, this usually indicates a mixed phase cloud is present. For mixed phase clouds the depolarization ratio equation becomes,

$$\delta(R) = \frac{\beta_i'(R)_\perp + \beta_w(R)_\perp}{\beta_i'(R)_\parallel + \beta_w'(R)_\parallel + \beta_w(R)_\parallel} \quad , \qquad (1.4)$$

where the primed β's represent the single-scattering volume backscatter coefficient, the unprimed β's represent the double backscattering coefficients for droplets (ice is assumed negligible in comparison) and the i and w represent ice and water particles (Sassen, 1991).

1.5 LARS

LARS objectives are to profile aerosols, cloud development, and cloud maintenance in order to study the effects clouds have on global radiative heat transfer. The LARS

instrument has a primary objective to investigate optical propagation conditions, scattering and extinction, in the lower atmosphere. LARS is to make measurements on cloud thickness, location, structure, ice and water droplet content, and distribution of aerosols. Using the depolarization ratio the cloud thermodynamic phase can be inferred. Deducing aerosol size is possible by using the Mie theory and the four wavelengths (the 94 GHz radar is included) of the system. Finally, the thickness, altitude, and structure of the clouds are determined through simple lidar resolution characteristics. In order to map the whole cloud, the system sits on a scanning platform that is capable of scanning a chosen solid angle within the upper portion of the hemisphere from 60 degrees off zenith (a 120 degree cone). For safety reasons, the platform will generally be operated above the 30 degree elevation angle, except where the airspace is controlled. A drawing of LARS's transmitter and receiver is shown in Figure 2. The transmitter and receiver are mounted on the table and are attached with the power supply and detectors, respectively, through an umbilical cord.

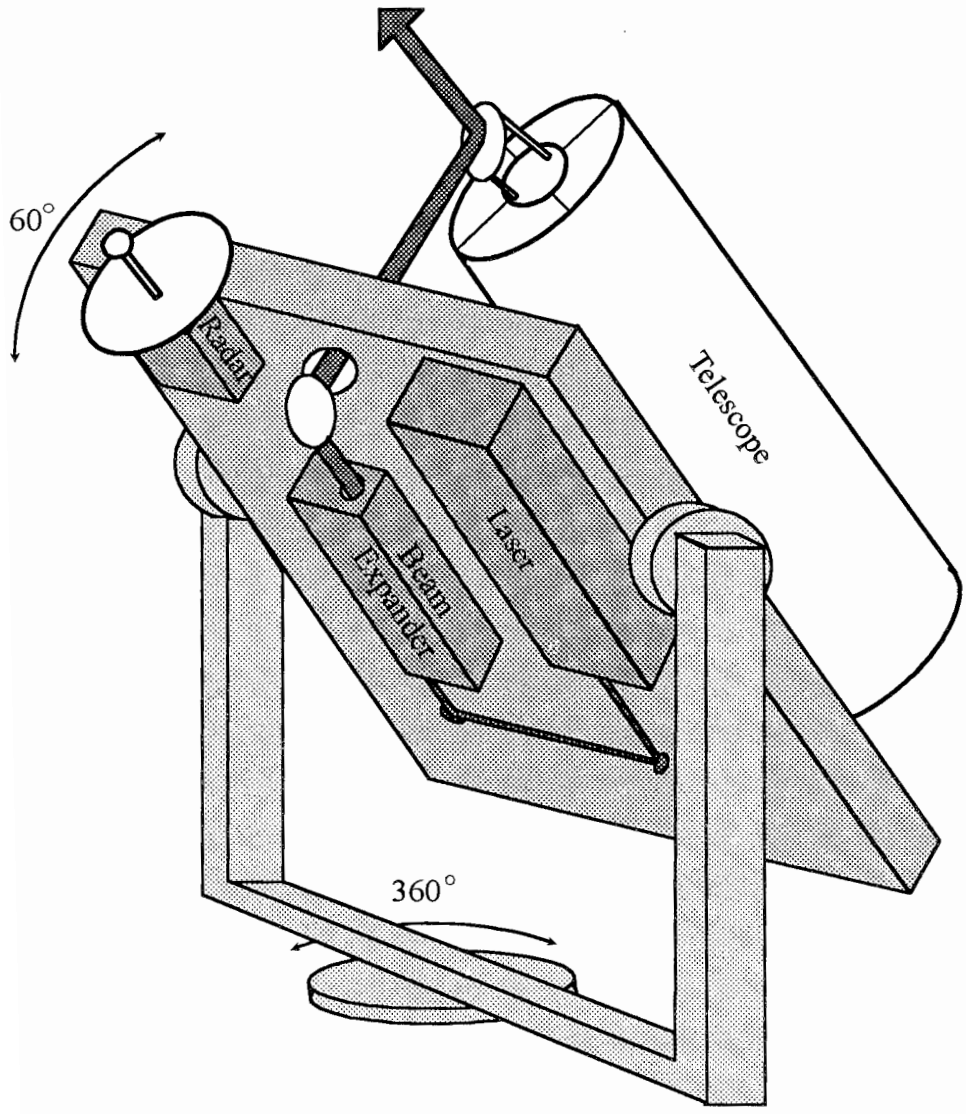

Figure 1.2. Drawing of the LARS transmitter and receiver

Chapter 2

The Transmitter

The transmitter subsystem of a lidar consists of several elements: a laser, several optics, a beam expander, and beam steering devices. These pieces of equipment must be carefully specified, modeled and assembled, to produce an efficient lidar. In addition, an energy monitor is needed to tune the laser harmonics and to record the laser stability during data acquisition.

Particular attention must be paid to other factors in the transmitter. Since LARS is a polarization lidar, the percent of polarization of the laser wavelengths in the outgoing beam must be known, because this percentage must be taken into account when determining the depolarization ratio. The warm-up period for the laser to reach a stable output must be found to optimize the performance and obtain meaningful data. Finally, an effort was made to find an antifreeze solution which could be used to prevent the water filled laser head from damage during freezing temperatures.

2.1 Transmitter Layout

The transmitter layout in Figure 2.1 (model numbers and characteristics are given in the following sections) is shown in approximately a 12:1 scale. The laser is triggered by the timing circuitry of the data acquisition subsystem to coordinate taking data and the laser pulsing. The laser pulse is directed off beam steering mirrors BS1 and BS2, which are highly reflective laser hard coated mirrors (each beam steering mirror mount contains the same type of hard coated mirror). From BS2 the pulse proceeds through a 6X beam expander to a

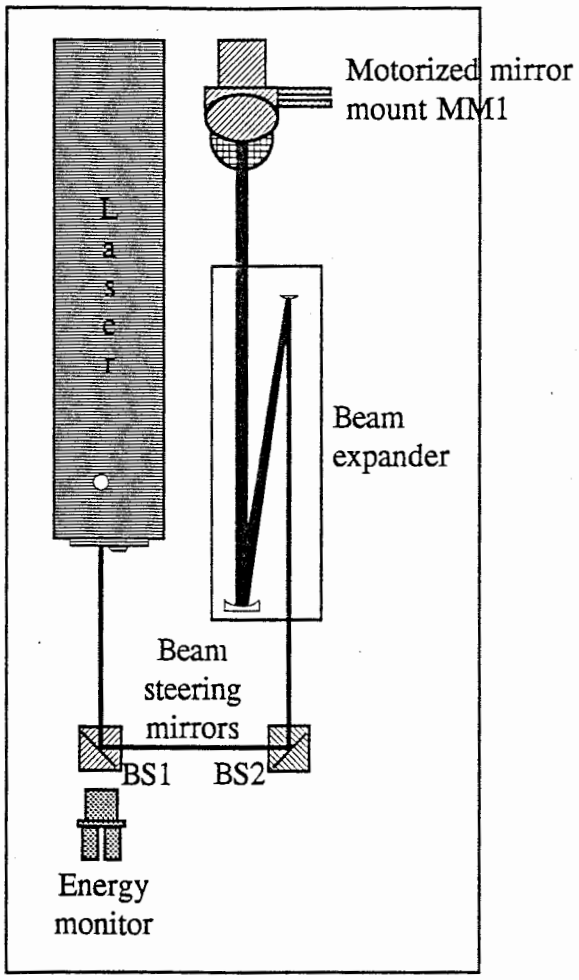

Figure 2.1. Transmitter layout

motorized mirror mount, MM1. From MM1, the beam is steered through a four inch hole in the table and onto a coarse adjustment mirror mount, MM2 (not shown). The beam is reflected by MM2, centered in front of the telescope's secondary, into the atmosphere. Sending the pulse through the table and off MM2 results in a coaxial lidar system which is preferable to a biaxial system. The coaxial arrangement provides an optically efficient design by allowing the laser pulse to be easy centered in the field of view (FOV) of the telescope. In addition, a biaxial arrangement is generally unsuitable for near field measurements under a few kilometers in range. Each part of the optical layout will now be discussed separately.

2.2 Laser Stability

The laser's stability is one issue that needs to be determined to characterize the LARS performance. If the laser output varies over the scanning volume or during a fifteen minute scan, then comparing and interpreting the data becomes difficult. Therefore, tests were conducted on the laser's output to determine the amount of time the laser needs to warm-up to reach stable output within 1 percent and then to assure that the output would remain stable.

The laser being used for LARS is a Continuum Surelite II-20 pulsed Nd:YAG laser. The laser has a 20 Hz pulse repetition frequency with a rod diameter of 7 mm and beam divergence of 0.6 mrad. The energy specifications of the laser are listed in Table 2.1 (Continuum, 1992). The energy stability given is from shot-to-shot for 99.9% of pulses. The power drift is determined from an average of eight hours. The manufacturers recommend that the warm-up period for the flashlamps be 20 minutes before the Pockels cell is turned on and laser operation begins.

The experimental tests of the laser's stability and warm-up period were designed to simulate data acquisition runs and procedures that are currently used in Penn State's LAMP lidar system. As an example, in the first run of the stability experiments (Table 2.2), test A, the flashlamps flashed for 20 minutes, the Q-switch was then opened and lasing proceeded for 2 hours, it was stopped for 5 minutes (flashlamps still running), then lasing occurred for another hour. This 5 minute delay would be normal for a lidar data acquisition run, since planes may cause a shutdown or other procedures may require the laser to be shut off for a short period of time.

Table 2.1 Continuum Surelite II-20 energy specifications

Wavelength (nm)	Energy (mJ)	Pulsewidth (ns)	Energy stability (± %)	Power drift (± %)
1064	500	5 - 7	2.5	3
532	225	4 - 6	3.5	6
355	90	4 - 6	4	6

Table 2.2 1064 nm laser stability tests

Test	Flashlamp warm-up (min)	Lasing (min)	Stop lasing, flashlamps on (min)	Return to lasing (min)
A	20	120	5	60
B	20	120	20	60
C	40	120	10	60

The results of tests A, B, and C are shown in Figures 2.2, 2.3, and 2.4 respectively.

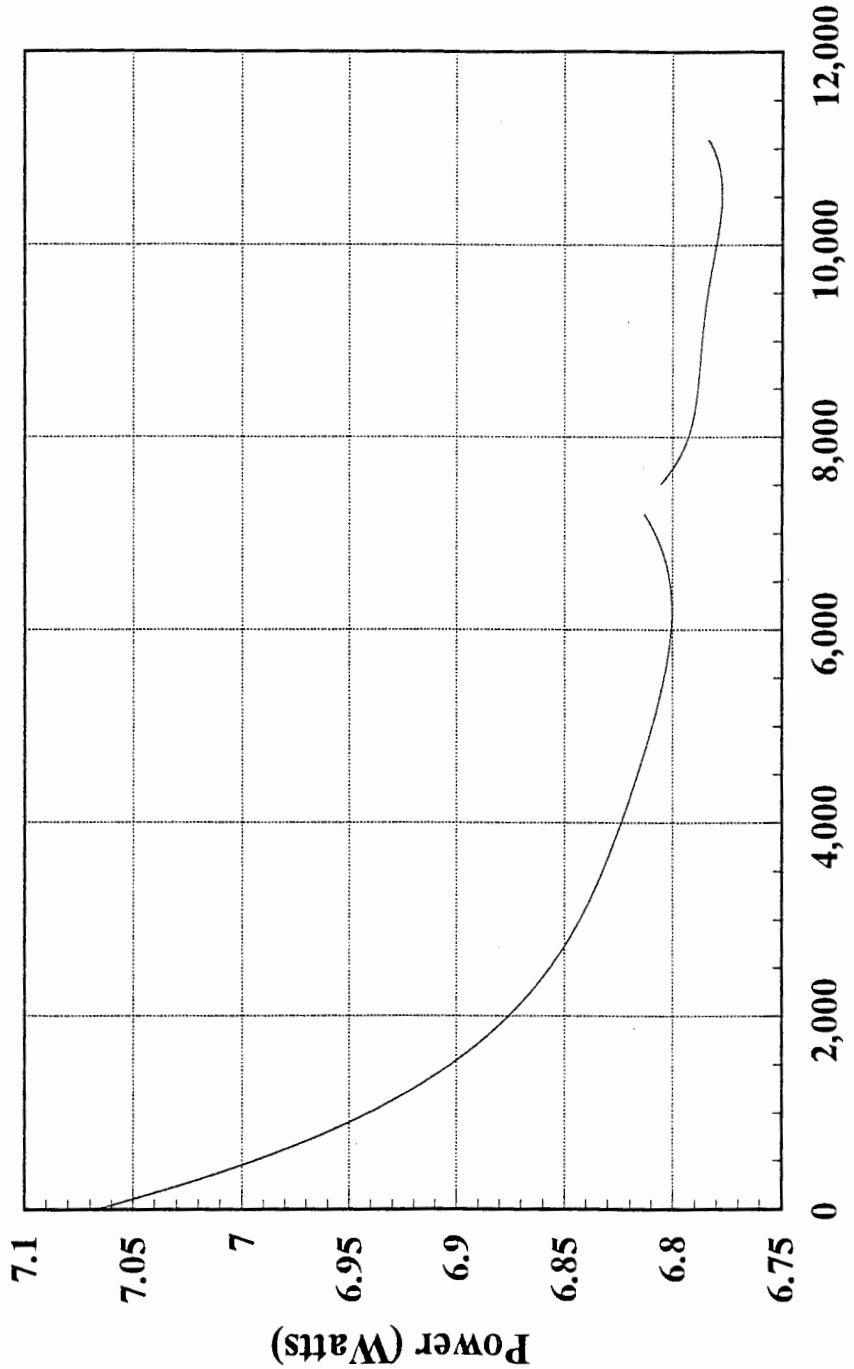

Figure 2.2. 1064 nm laser output (20 minute warm-up, 2 hours lasing, 5 minute stop, 1 hour lasing)

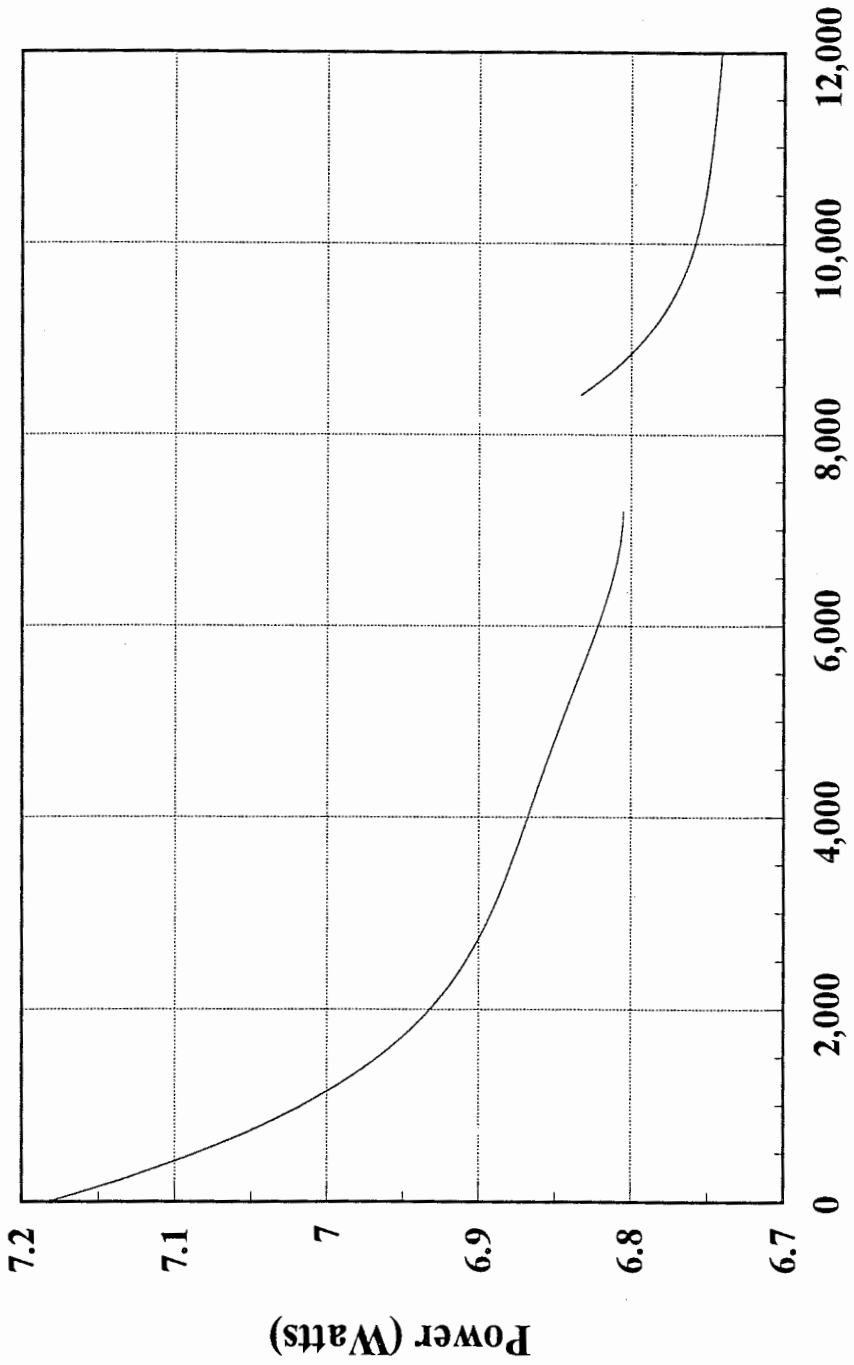

Figure 2.3. 1064 nm laser output (20 minute warm-up, 2 hours lasing, 20 minute stop, 1 hour lasing)

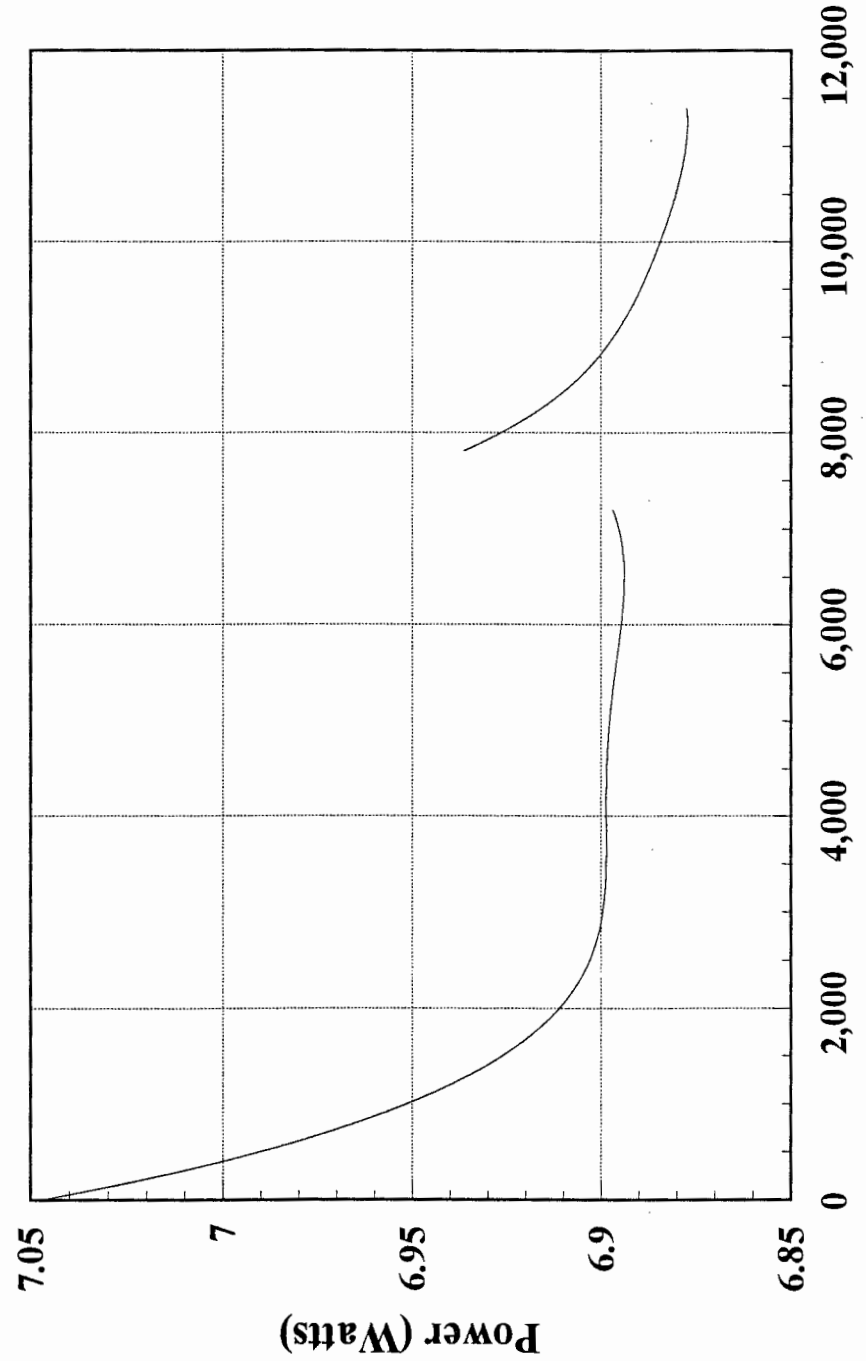

Figure 2.4. 1064 nm laser output (40 minute warm-up, 2 hours lasing, 10 minute stop, 1 hour lasing)

In Figure 2.2 (test A) the laser has an energy stability of 3.8 percent, slightly higher than the 2.5 percent the manufacturer specified. In addition, the laser needs to be operated for approximately 42 minutes before the laser stabilizes to within 1 percent. In Figure 2.3 (test B) the laser has an energy stability of 5.2 percent and takes 60 minutes to stabilize. In Figure 2.4 (test C) the laser is stable to 2.2 percent and takes approximately 15 minutes of lasing to reach a stable output within 1 percent (the flashlamps are flashing 20 minutes more than the other two tests). Test B has shown a case when it takes the laser longer to warm-up, this is the exception, when compared to the set of 10 other tests that were conducted. The reason all three cases show the decrease in power at the beginning is due to the fact that the laser cavity is not thermally stabilized and the back mirror alignment may be slightly off. As can be seen from the results the best time to run the laser with a deviation of 1 percent would be after the flashlamps have run for 40 minutes and the laser operating for another 20 minutes. Following this procedure before each run can assure that the laser has a stable output. In addition, a laser alignment should be conducted after the above procedure, since the laser cavity will then be thermally stabilized. Examination of the results of the tests where the lasing was stopped for several minutes in the middle of the test run indicates that upon start-up, the laser output stays within the 1 percent limit of stable output.

Next, tests were performed on the laser harmonics, 532 nm and 355 nm, since they are also used for cloud measurements. The 532 is critical because it provides the primary data for mapping the aerosol backscatter and the 607 nm Raman nitrogen return is shifted from the 532. The harmonic crystals used for producing these two wavelengths are attached to the end of the cavity of the laser and are peaked by angle tuning the crystal with an adjustment

knob attached to the harmonic generator. The adjustment knob sticks out of the laser housing about an inch and can be adjusted during lasing operations. The adjustment knob is very sensitive to touch, and a 1/8 of a turn can decrease the harmonic's output by up to 50 percent. The laser crystals are heated by the laser power dissipation and the manufacturer recommends running the 1064 nm pulses through the crystals for 5 minutes before peaking each harmonic generator. There are two types of crystals, I and II, that can be purchased for each harmonic. The type I crystal preserves the polarization of each of the previous wavelengths, but has a lower conversion efficiency than a type II crystal. The type II crystals may use a 1/4 wave plate as the entrance window or a different crystal material, thereby increasing the output of that harmonic, but these change the polarization of the entering wavelength. In addition, if a 532 type II crystal is used, there will be a 25 percent reduction in the 355 nm output. This reduction is produced by the 532 harmonic generator's 1/4 wave plate entrance window and crystal that causes the final 1064 nm polarization output to be 80 percent vertical and 20 percent horizontal. In LARS, the 532 is a type II crystal and the 355 nm is a type I crystal.

Tests were performed on the harmonic crystals to determine their energy stability. For the 532 crystal, the flashlamps were flashed for 20 minutes, lasing occurred at maximum power for 5 minutes and then the crystal was peaked. After the crystal was peaked, lasing continued for one hour, the crystal was peaked again, and lasing operation continued for another half hour; the crystal was again peaked and lasing operation continued again for a half hour. The lasing action was interrupted for 5 minutes (flashlamps flashing) and then enabled for another half hour. The 355 crystal was tested similarly, except the crystal was not peaked the second time (the laser ran for an hour before stopping for 5 minutes).

The results of the 532 and 355 harmonic tests are shown in Figures 2.5 and 2.6. The 532 has an energy stability of 4.3 percent, just over the 3.5 percent specified. In order to stabilize the harmonic to within 1 percent, approximately 45 minutes of lasing is needed. This, of course, is expected from the 1064 nm tests, since the 1064 nm output is not stable to within 1 percent until after the first 45 minutes. Also, when the crystal is tuned, it may take another 10 minutes for the output to stabilize. The 355 has an energy stability of 4.2 percent, near the 4 percent value specified by the manufacturer. It takes only 25 minutes to stabilize within 1 percent, though. The manufacturer maintains, that the crystals are more efficient when they are cool or when lasing begins rather than after lasing has warmed the crystals. It is recommended that the harmonics be peaked in between each 30 minute data acquisition run and checked after 5 minutes to see if they are drifting. Also, as with the 1064, the crystals are subjected to lasing for 20 minutes after a 40 minute warm-up in order to maintain a constant output.

2.3 Laser Cooling

Frequently, lidar systems are used in situations of freezing temperatures; whether it be on a field experiment, or during the local winter season. Therefore, water in any component may freeze, expand, and ruin equipment. The only LARS components containing water are the laser head, water lines, and laser cooling compartment. The laser head is the only location where water has no room to expand, and freezing will result in damaging the laser head.

In the winter of 1992, while LAMP was in its shipping container, the water froze in

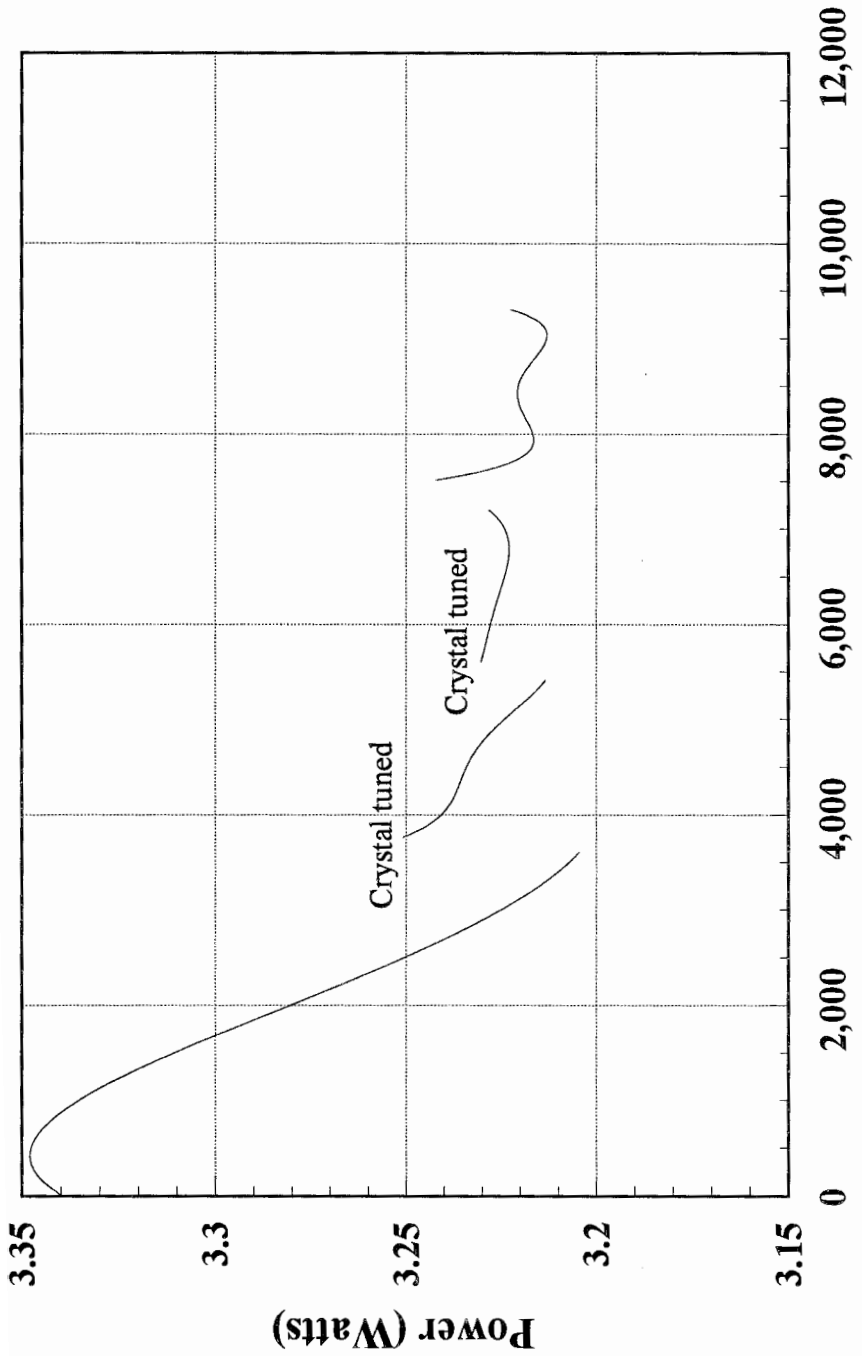

Figure 2.5. 532 nm laser output (20 minute warm-up, 2 hours lasing, 5 minute stop, 30 minutes lasing)

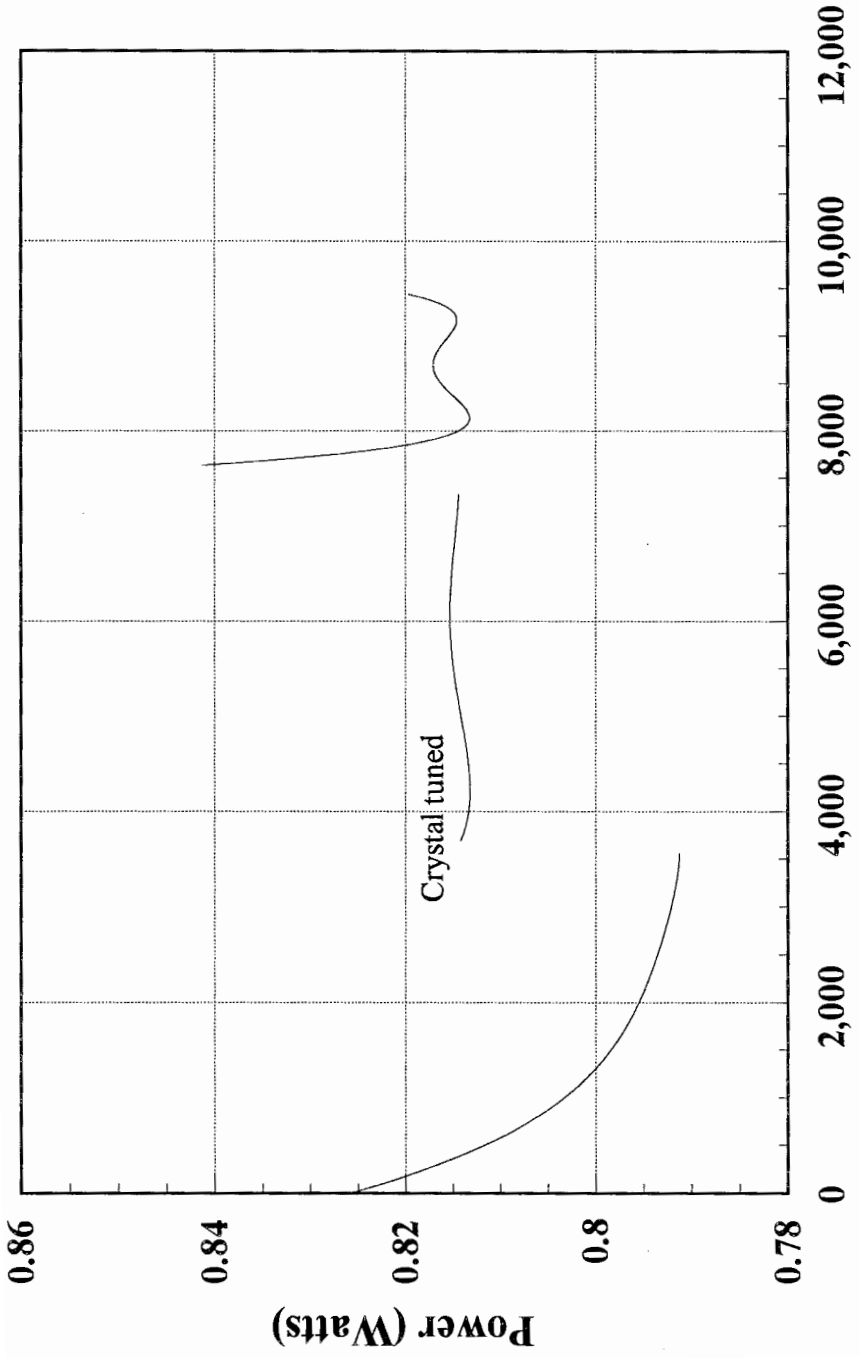

Figure 2.6. 355 nm laser output (20 minute warm-up, 2 hours lasing, 5 minute stop, 30 minutes lasing)

the laser head and resulted in extensive damage. Due to this event, it was recommended that an antifreeze solution be used in the laser cooling system so the laser would not freeze at temperatures down to -40 degrees Celsius. If a solution was found, it would need to have a high flash point, a low viscosity, be non-corrosive, optically stable against changes, and have a transmission spectrum similar to water. Two solutions were chosen, ethyl glycol and propylene glycol. The solutions would be mixed with water in proper proportions to produce an antifreeze capable of withstanding -40 degrees Celsius. The solution was then placed in the water holding container in the laser cooling system (Figure 2.7) without changing or removing any parts.

The ethyl glycol was the first solution to be tested in the laser system because it closely matched water's properties. The ethyl glycol solution spectrum compared with water is shown in Figure 2.8. Each fluid was measured while contained in a transparent fused silica cell with a Hitachi model U-4001 spectrophotometer. As can be seen, the ethyl glycol spectrum is similar to water with the major difference occurring in the ultraviolet region of the spectrum.

Laser power measurements were then taken on the 1064 nm output (Figure 2.9). The laser was first operated with just deionized water and resulted in a stable output around 9.75 Watts (letter A). At point B, the laser was restarted with the antifreeze solution in the cooling system. As can be seen the laser slowly decreases to an output of 9.4 Watts. At point C the laser was restarted and is stable at 9.2 Watts. Finally, at point D the laser power starts decreasing again and the laser was shut-off and inspected. The optics were not damaged and the flashlamp was new, so the laser head was removed and checked. Inside the laser head the

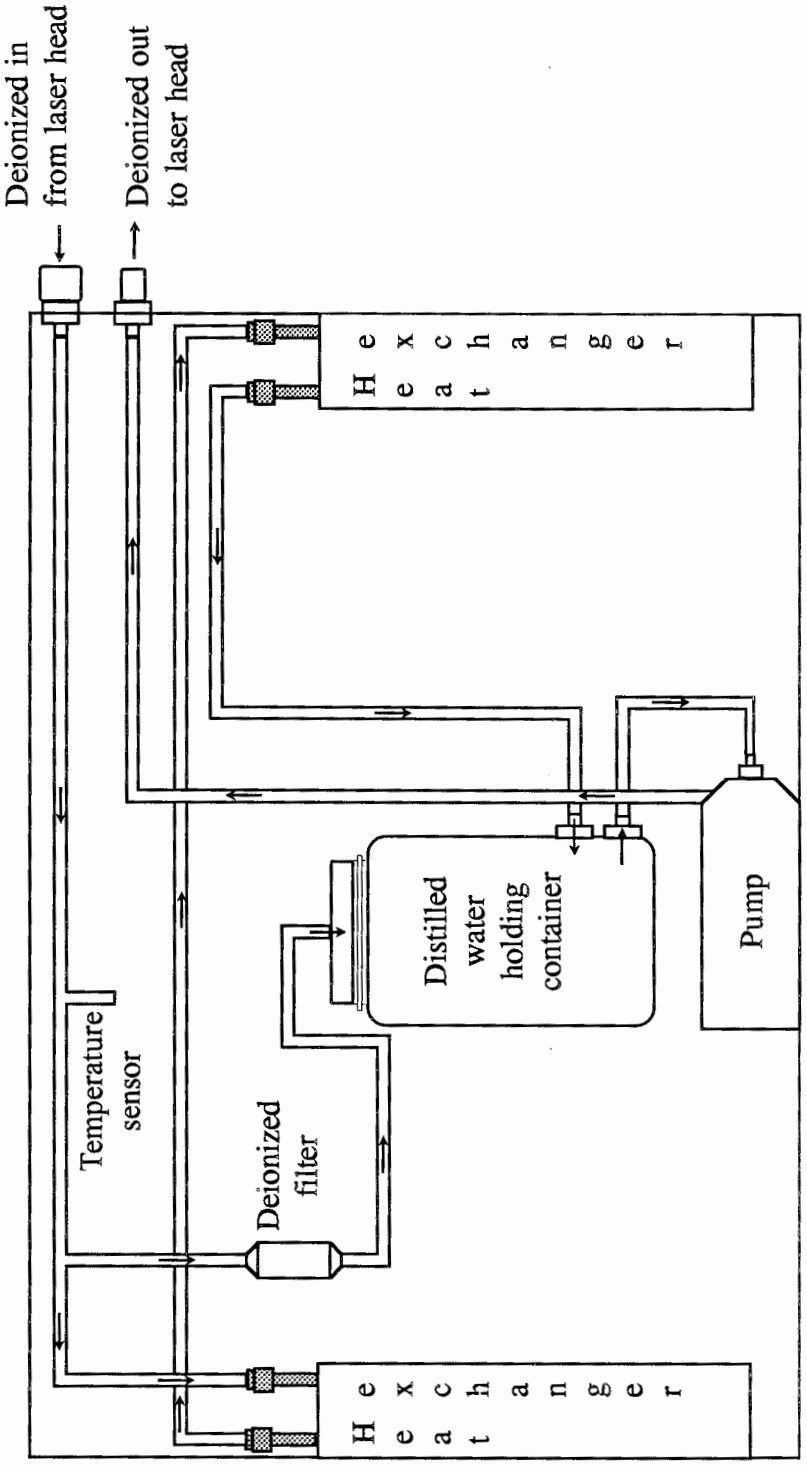

Figure 2.7. Surelite II-20 laser cooling system

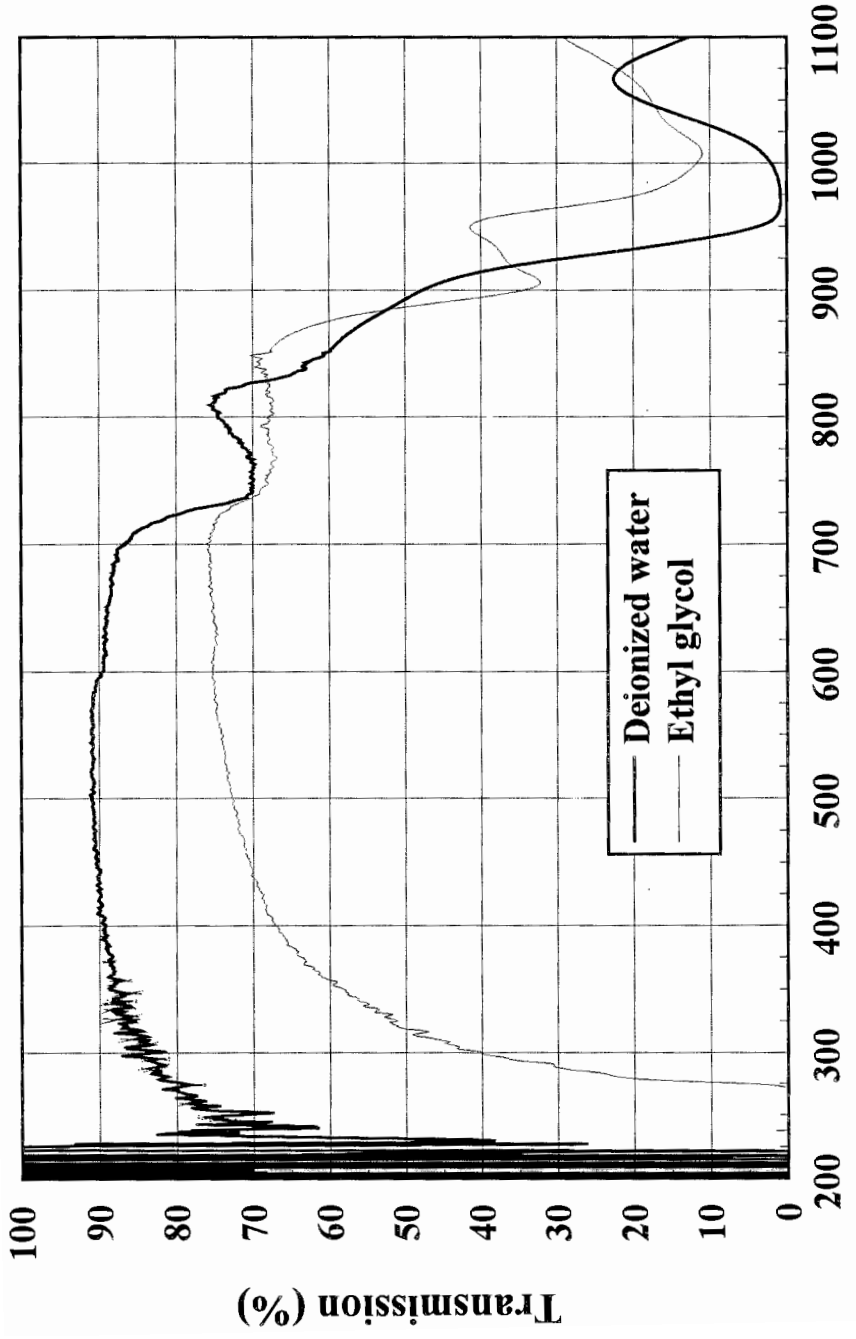

Figure 2.8. Comparison of spectra of deionized water and ethyl glycol solution

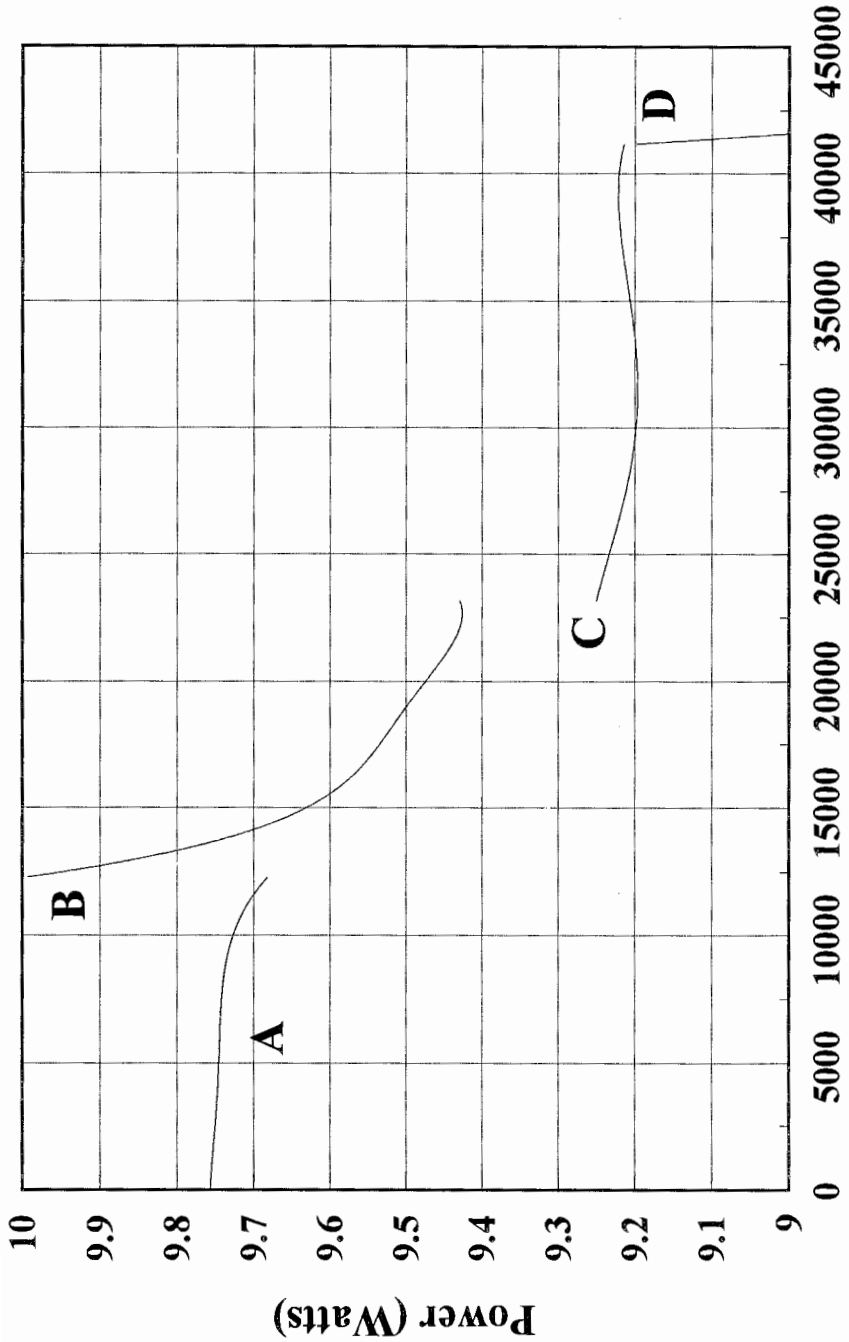

Figure 2.9. Laser power measurements before and during the addition of the antifreeze solution

magnesium fluoride diffuser, which holds the flashlamp and rod, was cracked. In addition, the diffuse reflecting powder and end RTV sealant looked rotted and was black, instead of its original white color. The laser head was damaged and needed to be replaced.

The results from this test have been examined and the following somewhat speculative conclusions drawn. At point B (Figure 2.9), the generally greater absorption of the antifreeze solution compared to water caused the loss in power of the laser, due to the absorption of flashlamp energy. The laser was operated 3 more times before the power went down further. The more localized heating in the laser head, along with the cooling of the laser system caused expansion and contraction of the magnesium fluoride diffuser, which finally resulted in the laser head cracking. It has been also suggested that the ethyl glycol was able to seep into the diffuse reflecting powder through the sealant, causing damage. In addition, Figure 2.10 shows how the ethyl glycol's spectrum changed after running through the laser system. Because the deionized filter was not removed from the cooling system (Figure 2.7), it seems that the ethyl glycol was being removed from the water by the filter.

Because of the expense of this laser head damage, no other solution was attempted. To keep the laser head from freezing during cold temperatures, heaters are now recommended (unless an antifreeze solution is found who's transmission spectra is matched to water).

2.4 Beam Steering

Once the laser beam has exited the laser, it needs to be steered into the centerline of the telescope field of view. This is accomplished through fixed and adjustable beam steering

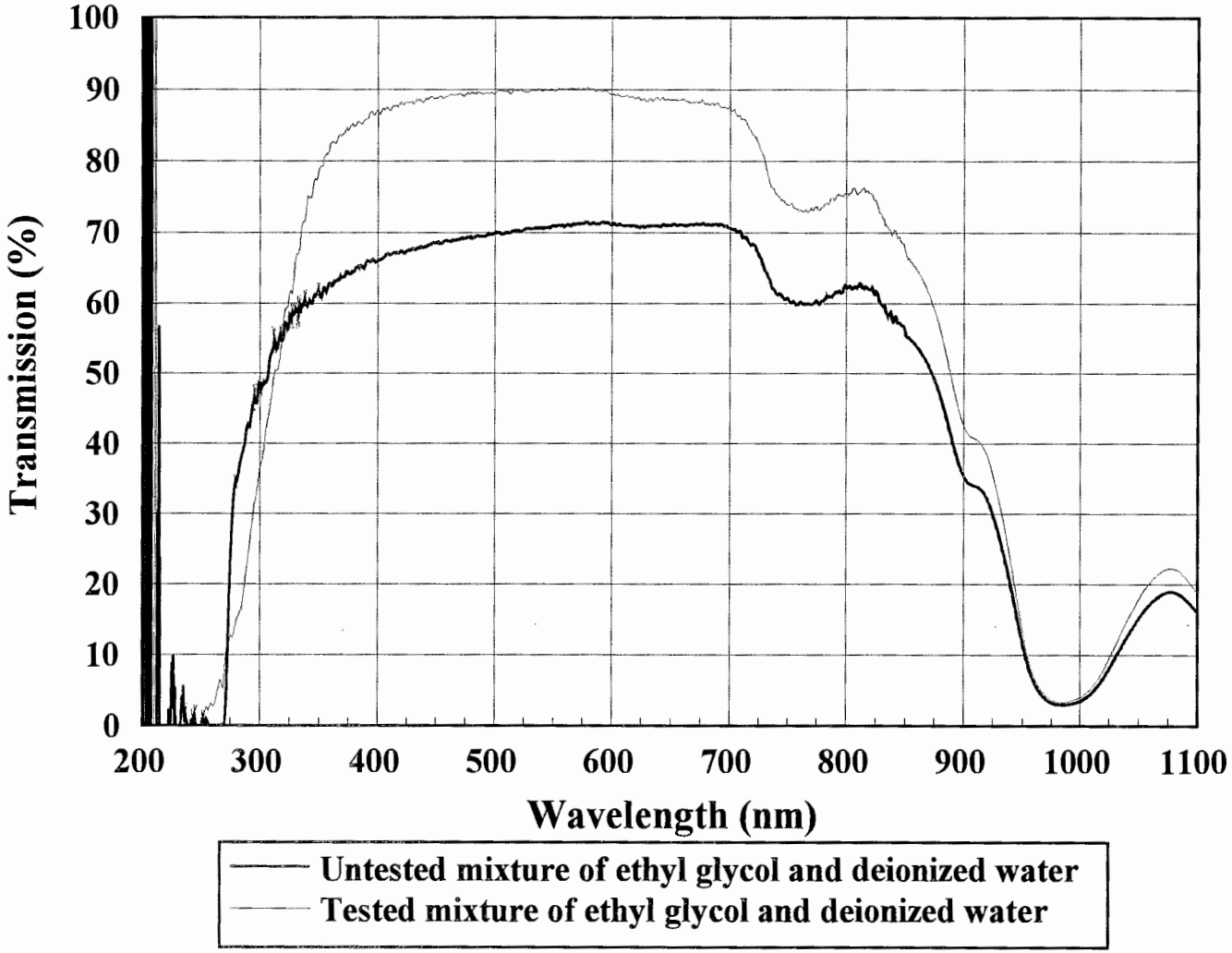

Figure 2.10. Comparison of spectra of laser tested and untested mixture of ethyl glycol and deionized water

mirrors. The transmitter layout is shown in Figure 2.1. BS1 is a 2 inch fixed mirror mount (Newport, LM-2R) positioned at a 45 degree angle. It holds a 2 inch high reflectivity laser hard coated mirror (all the mirrors used in the transmitter are coated identically) which directs the laser pulse to BS2. BS2 is a 2 inch kinematic (adjustable in the X and Y positions) mirror mount (Thor, KM2) and is used to position the beam on the optical axis of the beam expander. The setup was originally tried using a fixed mirror mount in BS2, to minimize the possibility of alignment changes. However, this is not practical since the mirrors are occasionally removed for cleaning, also alignment of the laser will result in mis-alignment in the optical path. Also, installing and removing any of the harmonic crystals causes small changes in the optical path.

The pulse passing through the beam expander is expanded six times, to 42 mm in diameter. After exiting the beam expander, the beam is reflected off a 4 inch motorized mirror mount (Oriel 18766) through a hole in the table. The mount is to be used to center the beam in the field of view of the telescope, because this mirror mount can be computer controlled and has a very fine angular resolution.

Finally, the beam goes through the four inch hole in the table and off a hard coated mirror in a 4 inch mirror mount (Newport, 625-RC4), MM2. MM2 has an orthogonal 10 degree angular adjustment range with a sensitivity of 2.5 arc sec. This coarse adjustment mirror mount is used to move the beam into the FOV of the telescope. This can be accomplished by looking at the detector fiber end and viewing the 532 return. Once MM2 is set and its micrometers are locked using a locking screw, then MM1 is operated to precisely center the beam in the FOV by maximizing the 532 nm return signal at a selected

high altitude.

Two points are considered in the setup of the beam steering. First, the two inch hardcoated mirrors (BS1 and BS2) are the most likely to be damaged by the laser since the beam is not expanded and the energy density at 1064 nm is around 260 MW/cm^2. Therefore, a riser block was designed so the laser pulse is directed not off the center of the mirror but at three quarters height of the mirror. This will allow the mirror to be rotated if it is burned. Also, it will allow the mirror mount to be raised, with spacers, so the mirror is at a new undamaged area and can once again be rotated.

Second, MM1's resolution needed to be determined to see how many steps of the stepping motor corresponded to the mirror's angular resolution. The information can be used to determine what the maximum number of steps the mirror will be able to be moved before the laser is out of the FOV of the telescope. This will be particularly useful when the mirror is incorporated into a computer controlled program that automatically centers the beam in the FOV.

Experimentally, the resolution of MM1 can be determined by directing the beam from a HeNe off the mirror and measuring the change in the HeNe's beam location, at a set distance, to the change in the step size of the motors. The angular resolution was found to be different for each axis since the stepping motors can be geared differently. For the X axis the angular resolution is 9.373×10^{-7} rad/step or 0.1933 arc sec/step ($\pm$ 1.5%) and for the Y axis the angular resolution is 1.05×10^{-6} rad/step or 0.2165 arc sec/step ($\pm$ 1.5%). This means that the FOV of the telescope, 0.575 mrad, could be covered, side to side, with a step count of approximately 615 steps.

2.5 The Beam Expander

The beam expander is used for two purposes. First, since the beam is expanded, the energy density of the laser beam is lower, reducing the possibility of the optics becoming damaged and reducing the likelihood of eye hazards. In fact, the expanded beam can be safely viewed when scattered from a diffuse target, but the unexpanded beam is not eyesafe from a diffuse target at close range. Second, and most important, the beam expander reduces the divergence of the beam in proportion to the expansion ratio. This reduced divergence produces two favorable operating situations; the beam will be fully in the telescope's field of view at lower altitudes and the spot size on the fiber will be smaller to allow improved coupling and alignment into the optical fiber. Even though the beam expander has not been received, it is on order at the writing of this thesis, and the specification are known.

The beam expander should be an off-axis reflective mirror design instead of a design using lenses. The lens beam expander would have to use expensive achromats because of dispersion, and would not have the same expansion and collimation for all three wavelengths.

The optimal expansion ratio is 6 times. In order to produce a coaxial lidar, the MM2 mirror mount is placed in front of the telescope's secondary mirror. Since the secondary mirror already obstructs a portion of the incoming signal, the mirror mount should be no larger than the secondary. If the mount is larger than the secondary, a smaller portion of the lower altitude signal will be collected. The mirror mount was then selected which holds a four inch mirror (clear aperture 3.6) at 45 degrees, resulting in an effective aperture of 2.55 inches. Therefore, at greater than a 6 times increase, the beam will cover too much of the effective aperture to allow alignment by the computer controlled mirror mount MM1. Since,

the larger the expansion ratio the smaller the divergence of the laser beam, the optimum expansion ratio is 6 times. This will result in the beam being in the FOV at around 1 kilometer (see section 3.4 for derivation) and the spot size on the optical fiber being its smallest.

Additionally, the coating for the beam expander mirrors needs to be effective at three wavelengths, 1064, 532, and 355 nm. The coating will also need to withstand 350 MW/cm^2 to account for localized hot spots in the laser beam. The wavelength coatings should be greater than 98% reflective for both S and P polarizations to ensure an efficient optical path and reduce the likelihood of coating and subsequent mirror damage. The ultraviolet coating, 355 nm, is the critical one because this wavelength will most likely cause damage first. The reason is related to the higher energy per photon. As the energy per photon increases, the photon's energy approaches the band strength of the coating, causing the coating to fail.

Finally, the polishing characteristics of the mirrors needs to be considered. The scratch/dig should be less than 20-10 to reduce the scattered light and assure proper coating of the mirrors. The wavefront error must satisfy 1/4 wave at 632 nm peak to valley optical path difference (OPD) error and 0.1 waves rms error OPD. Lord Rayleigh found that if the optical path difference is everywhere less than a quarter of the wavelength of the light, the image will not be noticeably imperfect; this is commonly known as the Rayleigh limit of permissible imperfection (Kingslake, 1983). The ratio of the peak to valley OPD to rms OPD should be greater than 4:1 to ensure that the wavefront error does not have large angles that will scatter and diverge the laser beam more than usual.

2.6 Energy Monitor

The energy monitor is used for two reasons. First, the energy monitor can be used to peak the output from the harmonic crystals of the laser. Second, the energy monitor can record the pulse energy at each wavelength to help interpret the lidar return signal. In addition, because the energy monitor is located behind one of the mirrors, a large increase in the output signal of the energy monitor, will mean that the hard coated mirror is burned and will need to be rotated.

A diagram of the energy monitor is shown in Figure 2.11. The energy monitor is placed behind beam steering mirror BS1 (Figure 2.1). Even though the mirror is coated, the coating is not 100 percent reflective and will transmit a certain percentage of light (see Figure 2.15). The energy monitor is designed to measure all three laser wavelengths. The light that is transmitted through the mirror will go through a center entrance aperture, which allows the beam to be aligned at roughly the same spot every time (within 0.1 inch). The light strikes a diffuser, which diffuses the light as a Lambertian source (intensity distribution follows Lambert's Cosine Distribution Law). The diffused light should enter all three wavelength monitoring tubes equally, since each detector is equally spaced from the center. Each detector is placed into a one inch tube that houses a neutral density filter (to lower the energy), a filter centered at one of the laser wavelengths, and a photodetector. The photodetector used is an EG&G HUV-1100 and its spectral response range is from 180 to 1150 nm. The circuit used for the photodetector (Figure 2.12) was taken from the EG&G Judson silicon photodetector manual and includes the capability of amplifying the photodetector's signal. The photodetector's signal is then sent over a coaxial cable to the

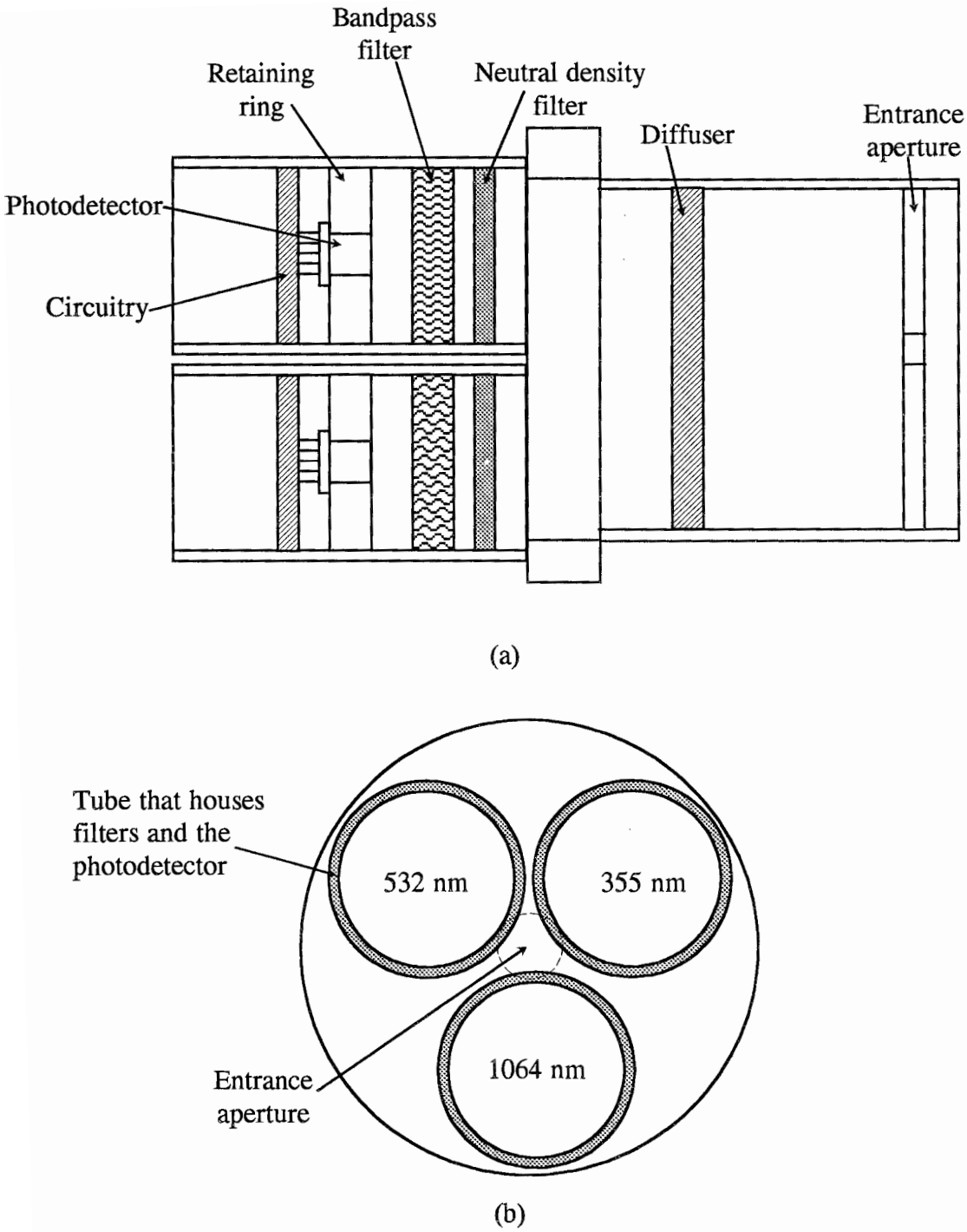

Figure 2.11. Energy monitor (a) cut-away side view and (b) back view

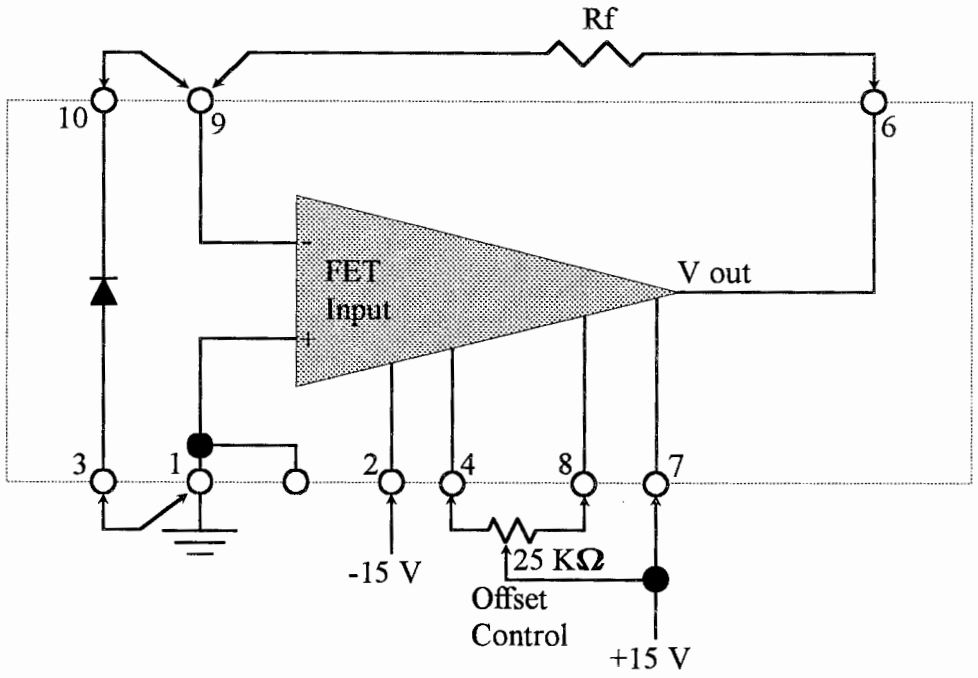

Figure 2.12. Suggested electrical circuit for the HUV-1100BQ photodetector (EG&G Judson, 1990)

oscilloscope. The resulting waveform on the oscilloscope will increase (decrease) in amplitude with an increase (decrease) in the pulse energy at each wavelength. This is not an absolute measurement, but a relative measurement since another commercial power meter will be used to calibrate the LARS monitor. For now, the energy monitor reading is displayed with the oscilloscope to aid in a quick peaking of the laser harmonics.

The energy monitor output was tested with a digitizing oscilloscope. The 1064 nm wavelength was found to need a neutral density filter with an optical density of 9 in order not to saturate the photodetector. The photodetector goes into saturation at 9 volts output. The output of the photodetector was taken into the 1 megaohm channel of the scope. The offset voltage used for the photodetector was $\pm$ 11 volts, instead of the $\pm$ 15 volts recommended, and the feedback resistor, Rf, was set at 100 megaohms (instead of the 200 megaohms recommended). Figure 2.13 shows the output of the energy monitor versus the laser power for 1064 nm (also shown is the linear fit). The wattage of the laser was checked with a calibrated Molectron PM30V1 power meter. The energy monitor is shown to closely match the linear fit with a calibration of 0.787 watts/volt. For the 532 nm wavelength, a neutral density filter of 5 was used and an offset voltage of $\pm$ 11 volts was used. Figure 2.14 shows the output of the energy monitor versus the laser power for 532 nm (also with the linear fit). The energy monitor is again shown to closely match the linear fit with a calibration of 0.483 watts/volt.

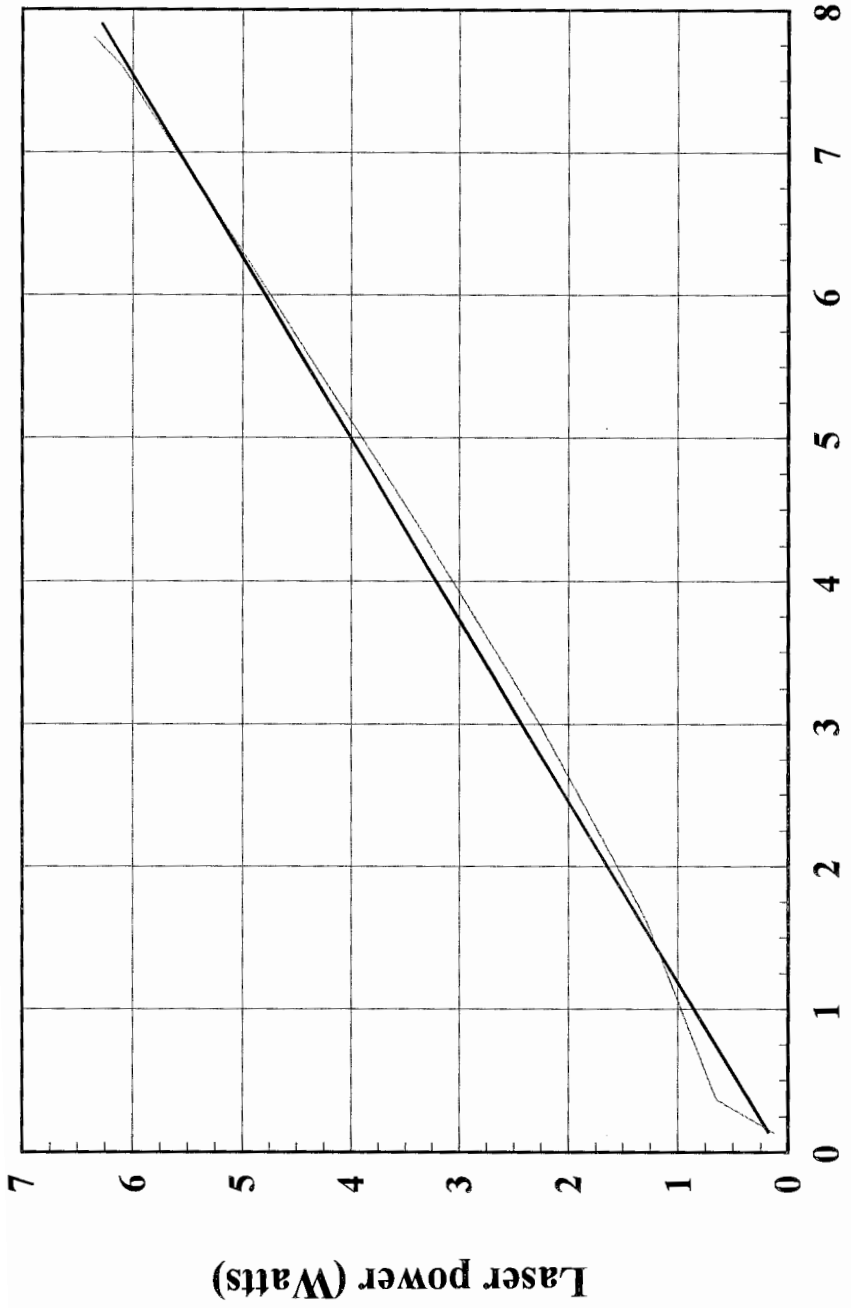

Figure 2.13. 1064 nm output from the energy monintor into a 1 megaohm digitizing oscilloscope (with linear fit)

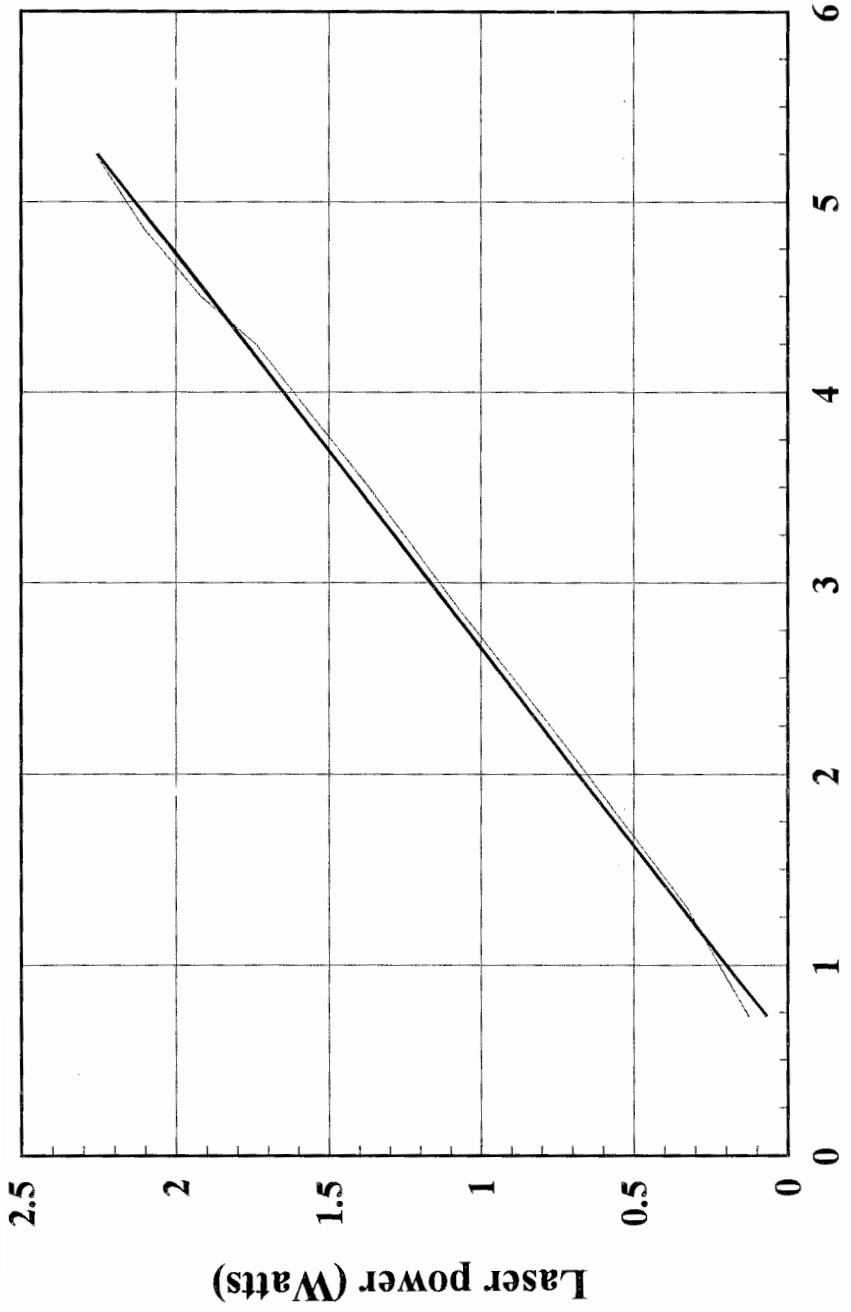

Figure 2.14. 532 nm output from the energy monitor into a 1 megaohm digitizing oscilloscope (with linear fit)

2.7 Polarization

The LARS system is a polarization lidar, therefore, the output wavelengths should be polarized in the S or P direction. If the wavelengths are partially polarized, the depolarization ratio can be difficult to interpret unless the wavelength's polarizations are accurately determined. Measuring the percentage of polarization at each wavelength will provide the information needed to interpret the return signal.

The manufacturer states that the polarization of the laser for 1064 is greater than 99 percent horizontal, the 532 is greater than 95 percent vertical, and the 355 is greater than 95 percent horizontal. But, since the 532 harmonic uses a type II crystal, the 1064 switches to approximately 80 percent vertical and 20 percent horizontal after exiting the 532 crystal (the 532 is still greater than 95 percent vertical). In order to determine the exact amount of polarization and the change in polarization off of each 45 degree mirror, a Glan-Thompson polarizer was used to measure only the 1064 nm polarization. The reason only the 1064 is measured is because in order to split off the harmonic wavelengths, two 45 degree harmonic beamsplitting mirrors would need to be used. These mirrors will partially depolarize the harmonic's polarization. In addition, due to this rotation, another Glan-Thompson polarizer would be needed to clean up the polarization to 100 percent of either S or P.

The polarization test involved placing the Glan-Thompson polarizer in the laser path and using a power meter to measure the polarizer's outputs for the S and P polarizations. Next the polarization was measured after the 1064 was reflected off a 45 degree hard coated mirror. The mirror is considered to be a P mirror since the polarization of the 1064 nm output is horizontal. Finally, the laser was rotated on its side to change the laser's polarization

to vertical and make the mirror a S mirror (since the LARS transmitter setup consists of S and P mirrors). The laser was reflected off the S mirror and the percent change in polarization measured.

The laser output was measured to be 99.5 percent horizontal. The P mirror (at 45 degrees) changed the polarization by 5.33 percent to 94.2 percent when the laser was reflected off it. The S mirror (at 45 degrees) changed the laser's polarization by 4.92 percent to 94.6 percent. If the 1064 was the only wavelength being used, starting at 99.5 percent horizontal, the final laser pulse's polarization after leaving the transmitter (due to two S and two P polarization mirrors in the system) would be 82.11 percent horizontal and 17.89 percent vertical (not including the beam expander). This calculation assumes that the polarization changes after being reflected by the mirror upon leaving the last coating layer.

2.8 Optical Efficiency

As can be seen from the lidar equation (1.2) the more transmitted photons that are sent into the atmosphere, the greater the return signal will be. The laser efficiency is determined by how well the harmonics are peaked and has already been discussed in section 2.2. The optical efficiency of the transmitter can not be changed (unless different coatings are used), but it needs to be determined to model the performance of the system.

The transmitter layout is shown in Figure 2.1. The four hard coated mirrors (BS1, BS2, MM1, MM2) were all coated in the same batch, therefore, only one of the two inch mirrors was tested in the spectrophotometer. The reflection scans of the mirror (Figure 2.15) include S and P polarization measurements, since the optical path polarization state changes

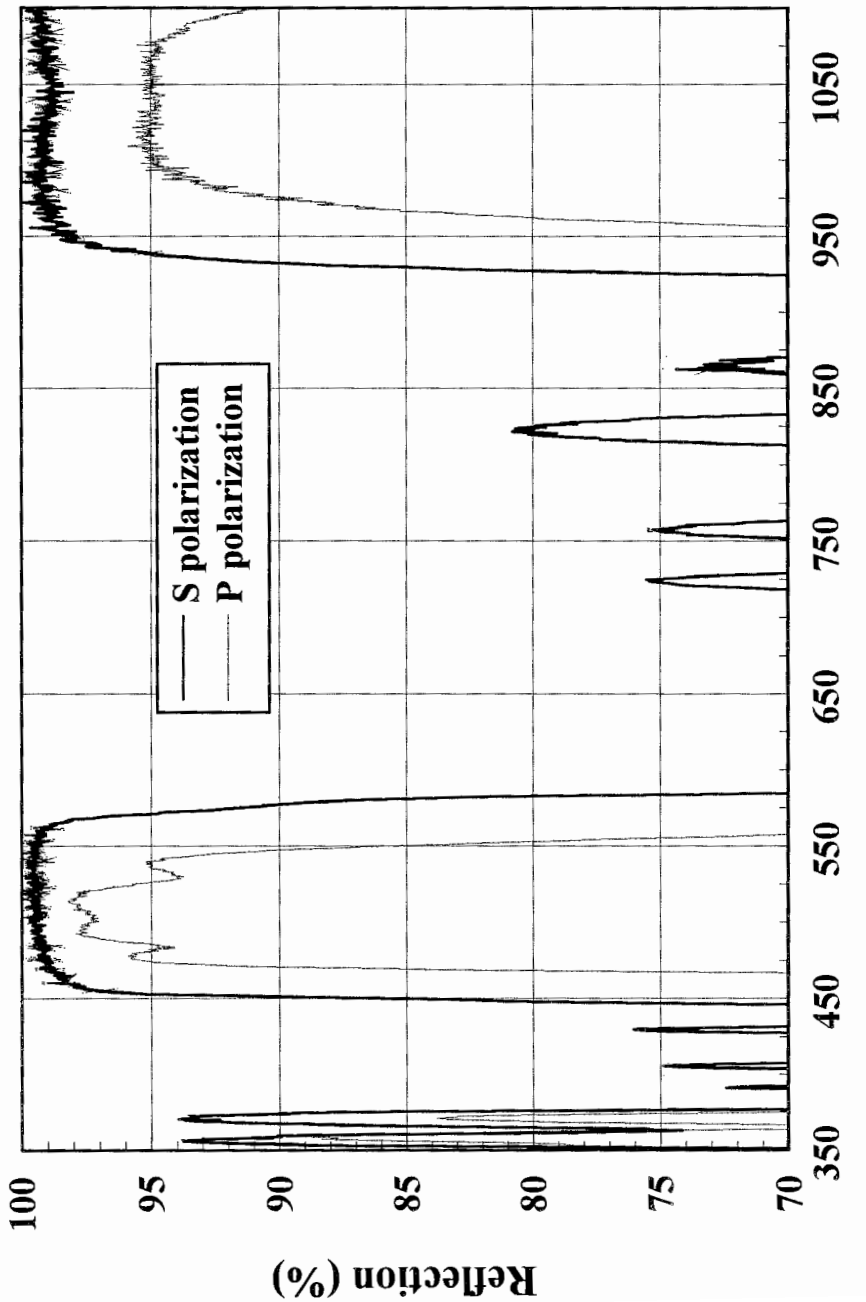

Figure 2.15. Measured reflection of the beam steering hard coated mirrors

from mirror to mirror. Table 2.3 shows the results of the spectrophotometer scan. In addition to the mirrors, the beam expander should be included in this test. Because, the beam expander has yet to be delivered, the specifications given in section 2.5 will be used.

Table 2.3. Transmitter optical efficiency

Wavelength (nm)	Hard coated mirror S polarization (% reflected)	Hard coated mirror P polarization (% reflected)	Beam expander mirror specifications (% reflected)
1064	99.11	95.04	96
532	99.60	94.24	96
355	92.62	81.80	96

Using the polarization characteristics of the 1064 nm wavelength, and assuming the polarization of the laser pulse off the 45 degree mirrors do not change until after it is reflected from the final coating layer, the efficiency of the transmitter will be calculated. If the output energy at 1064 nm is 100 mJ, 99.5 mJ will be P polarized and 0.5 mJ will be S polarized. The system is composed of two P mirrors, two S mirrors, and the beam expander. The final output from the last mirror will be 69.92 mJ of P polarized light and 14.62 mJ of S polarized light. Adding these two polarizations together gives a total transmitter efficiency of 84.54 percent. If the calculation was made just multiplying 100 mJ by the two P mirrors, two S mirrors, and the beam expander, the efficiency will be 85.18 percent. The difference, when taking the polarization effects into the efficiency calculations, is negligible. Therefore, an approximation will be made for the 532 and 355 nm wavelengths. Again, using two P mirrors, two S mirrors, and the beam expander, the transmitter efficiency for 532 nm will be 84.58 percent, and for 355 nm the efficiency will be 55.10 percent.

Chapter 3

The Receiver

The receiver subsystem's main purpose is to collect the backscattered photons from the outgoing laser pulse and transfer the signal efficiently to the detector box. The receiver subsystem of the LARS lidar is composed of several items: a telescope, a polarization divider box, and two fibers used to transfer the S and P polarization signals to the detector box. These three pieces of equipment require several mechanical and optical considerations in the design of the receiver, and these will be discussed in this chapter. In addition, the optical efficiency of the receiver and the field of view of the telescope will be addressed.

3.1 Optical Layout

The receiver layout in Figure 3.1 is shown in approximately a 12:1 scale. Mirror mount MM2 is located on the receiver side of the optical table to produce a coaxial lidar (discussed in section 2.1). The laser pulse is reflected off MM2 and into the atmosphere. The backscattered photons are collected by the telescope and directed into the polarization divider box. The polarization divider box is attached to the back of the telescope and is composed of lenses, a polarization splitter cube, and optical mounts. The polarization divider box splits the return signal S and P polarizations and directs each polarization signal to an optical fiber. The signal from each fiber is transferred to the detector box.

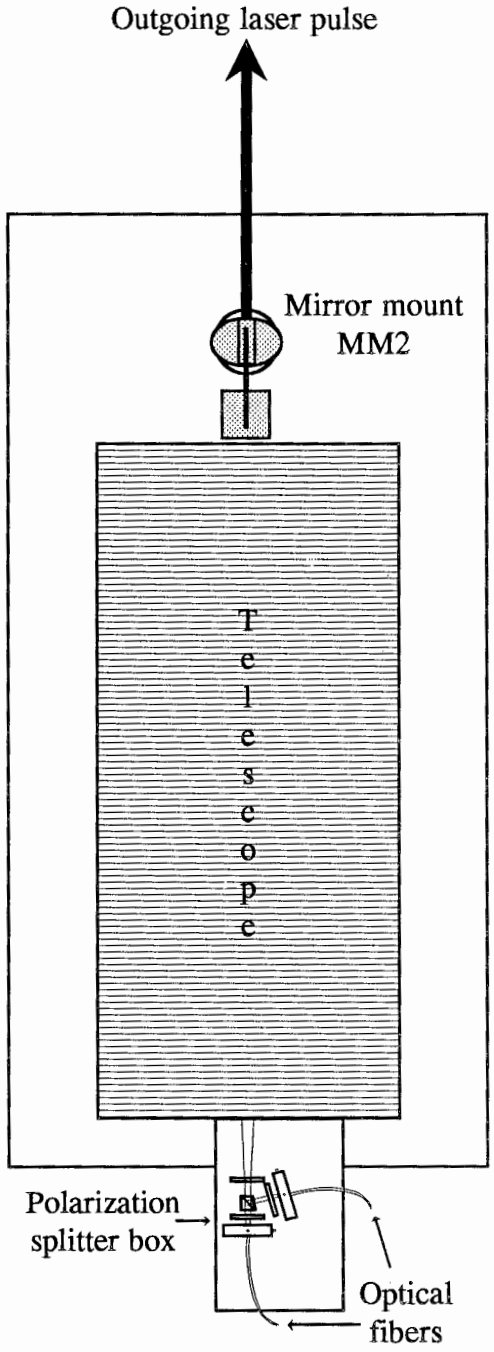

Figure 3.1. Receiver layout

3.2 The Telescope

The function of the telescope is to collect the backscattered photons from the outgoing laser pulse. Depending on the performance required, there are several design considerations that need to be taken into account. These design considerations include: the type of telescope, size of the collecting optics, f-number, and back focal length.

The telescope chosen was a Ritchey-Chretien Cassegrain, 16 inch diameter, f/7.8, 43 inches length, motorized secondary, with a back focal length of 10 inches (Optical Guidance). The Ritchey-Chretien Cassegrain telescope was chosen because it is a polarization preserving telescope which is relatively short and light weight. Therefore, backscattered photons will not be depolarized by the telescope before they reach the polarization divider box. Also, for this class of Cassegrain telescopes, the Ritchey-Chretien has a relatively short length compared to its diameter. This small length is needed so that the scanning optical table is not too heavy, wide, or mechanically clumsy. The 16 inch diameter was chosen because it is a diameter that has been used in the LAMP lidar and it was considered the largest size that was light enough to be easily maneuvered. Obviously, there is an important trade-off between the diameter and number of backscattered photons collected. The focal length was chosen so the field of view of the telescope, if using a 1 mm diameter fiber, would be less than 1 mrad and so that the overall length of the telescope is less than 46 inches (to fit on the optical table). A motorized secondary, instead of a fixed secondary, was chosen to allow the back focal plane to be moved in order to simplify the position alignment of the signal in the polarization divider box. The back focal length, when the secondary is in its original position is 10 inches, and is adjustable, using the motorized secondary, from 14 inches to 6 inches. This movement

is necessary since there is limited space on the back of the telescope and the polarization divider box must be fixed in position on the optical table.

3.3 The Polarization Divider Box

The polarization divider box is used to split the return signal S and P polarizations. This is performed so that the information from the cloud ice/water phases or multiple scattering conditions can be detected. The divider box consists of lenses, a polarization splitting cube, and optical mounts. Once the return signal polarizations are split, each polarization signal is sent through an optical fiber to the detector box.

The layout for the polarization divider box is shown in Figure 3.2 (approximate 2:1 scale) and an illustration of the optical path is shown in Figure 3.3. Assuming the laser is centered in the field of view of the telescope, the return signal converges toward the focal plane of the telescope. Ahead of the focus, a fused silica plano-concave lens (Pl-Cc) is used to collimate the return signal. This is accomplished by setting the focal plane of the negative lens at the distance of the focal plane of the telescope. The lens is oriented with the plano face pointed toward the telescope because this will collimate the light with less aberration.

The collimated light is then sent through a polarization splitting cube to split the S and P polarizations. The P polarization will proceed straight through the cube, while the S polarization will be reflected in the cube, and sent out a side face at an angle of 75.2 degrees to the input optical axis. The signal is still collimated after exiting each face of the cube. From the cube, the collimated light is passed through a fused silica plano-convex (Pl-Cx) lens and focused into an optical fiber. The optical fiber is placed at the focal point of the lens to

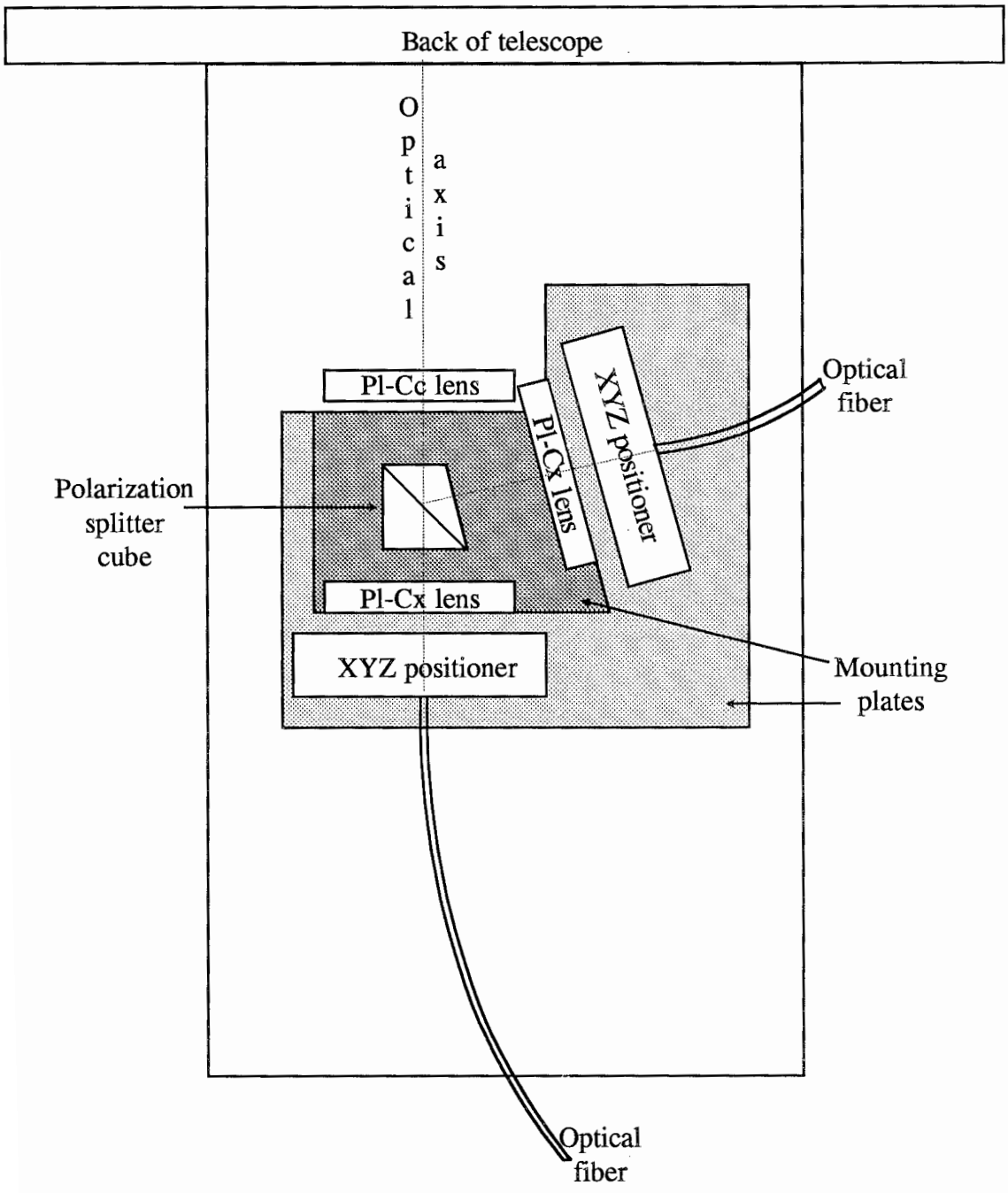

Figure 3.2. Polarization divider box

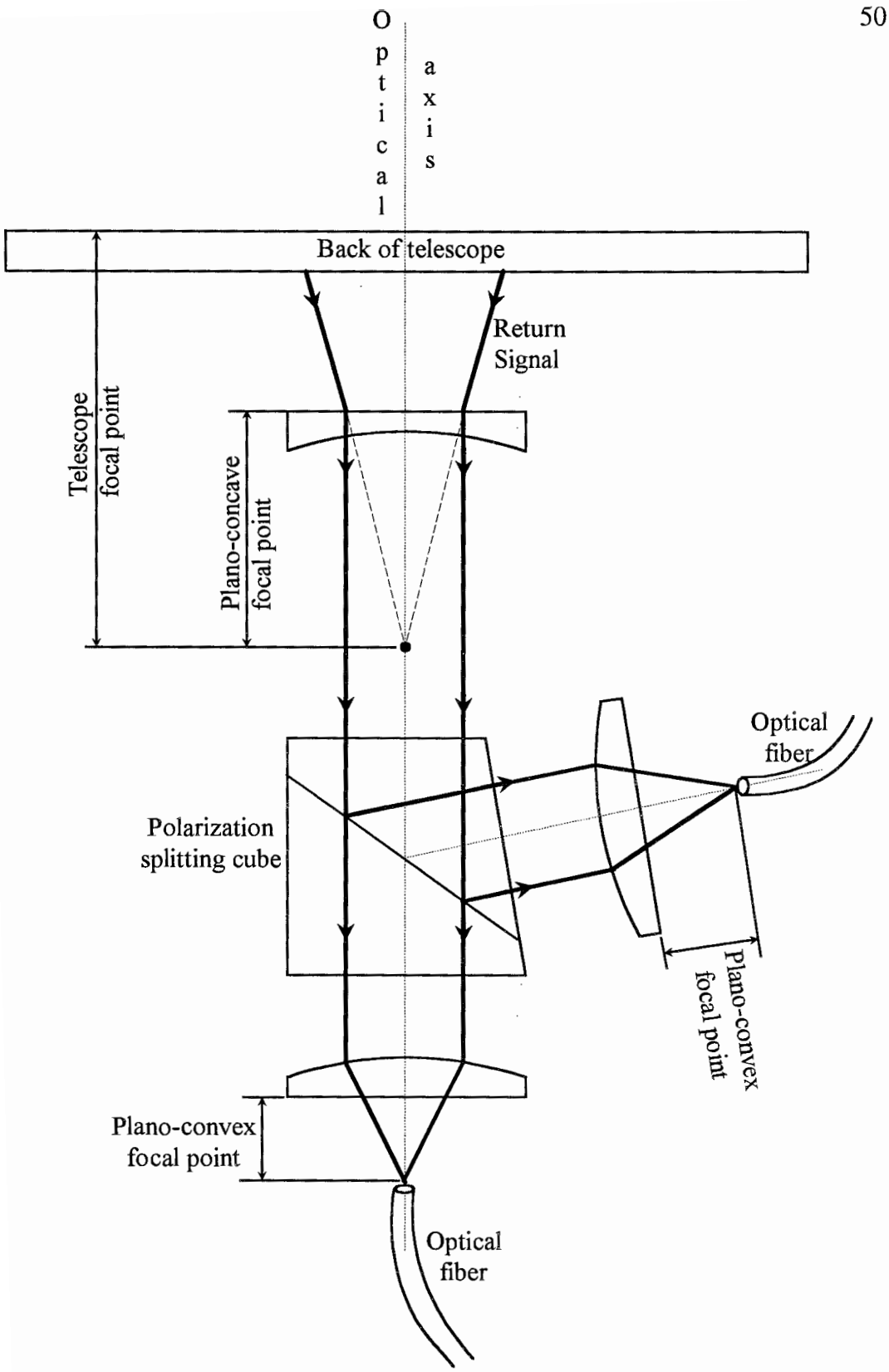

Figure 3.3. Illustration of the optical path of the polarization divider box

collect the most signal. As before, the plano side of the lens is oriented toward the fiber to focus the light to a tighter focal spot. The optical fiber is screwed into a mount that screws into an XYZ positioner. The XYZ positioner is used to accurately locate the fiber at the lens' focal point.

There are several optical concerns that had to be considered in the polarization divider box. First, fused silica lenses (instead of glass) are used because of their high transmission in the UV. Second, because of dispersion, the focal length of the lenses for each of the four wavelengths detected are different. The dispersion influence has been minimized by selecting this configuration of negative and positive lenses. This dispersion effect influences at what altitude each wavelength will completely enter into the FOV of the telescope. Calculations of what altitude each of the wavelengths will come into the FOV are discussed in the next section.

3.4 Receiver Optical Considerations

There are several important considerations to address when combining the polarization splitter box with the telescope. First, the field of view of the telescope needs to be larger than the divergence of the laser, or else the return signal will be nonlinear. Second, the clear aperture of the polarization splitting cube is only 12 mm. Third, the numerical aperture of the fiber is approximately 0.34 (allows a maximum entrance angle of 19.88 degrees). Finally, dispersion, the change in index of refraction with wavelength, must be considered for the range of wavelengths used.

First, the field of view of the telescope is found. Examination of Figure 3.3 indicates

that the light exiting the plano-concave lens is collimated. This is accomplished by placing the negative lens ahead of the focal plane of the telescope and then matching the focal point of the negative lens with the telescope's focal plane. This arrangement essentially produces a reverse beam expander. The input of the beam expander is the 16 inch diameter of the telescope, and the output diameter is determined by a ratio involving the telescope and concave lens focal lengths (derivation follows). The output diameter, though, must fit the clear aperture of the polarization splitting cube. The focal length of the telescope is 3.17 meters. To find the focal length, f, of the negative lens we use the lensmaker's formula:

$$\frac{1}{f} = (n-1)\left(\frac{1}{R_1} - \frac{1}{R_2}\right) + \frac{t_c(n-1)^2}{nR_1R_2} \quad , \tag{3.1}$$

where n is the index of refraction of the lens at a certain wavelength, R_1 and R_2 are the radii of curvature of the lens and t_c is the thickness of the lens. For a thin plano-concave lens $R_1=\infty$ and

$$f = -\frac{R_2}{n-1} \quad . \tag{3.2}$$

Using R_2 = 27.4 mm for the concave lens, and n = 1.46071 at 532 nm, the focal length is -59.47 mm. This focal length was selected so that the diameter of the collimated light leaving the lens would fit the clear aperture of the polarization splitting cube and because this focal length was commercially available.

Assuming the light is from an infinite source and using similar angles, the output diameter at the concave lens can be found to be equal to 7.624 mm. This diameter will fit the 12 mm clear aperture of the polarization splitting cube and allow for a small mis-alignment. Using 406.4 mm (16 inch telescope diameter) as the input beam, the expansion ratio is 53.31 times. The field of view of the telescope then will be due to the divergence of the combination of the fiber and the plano-convex lens divided by the expansion ratio.

The focal length of a thin plano-convex lens ($R_2 = \infty$) is,

$$f = \frac{R_1}{n-1} \qquad (3.3)$$

Using n for 532 nm and R_1 = 15 mm, the focal length of the convex lens is 32.6 mm. When the fiber is placed at the focal point of the convex lens, the fiber's 1 mm core becomes the field stop of the system. The inverse tangent of 1mm/32.6mm determines the field of view (divergence) of the convex lens/fiber combination and equals 30.67 mrad. Dividing the 30.67 mrad by the 53.31 expansion ratio, yields a telescope field of view of 0.575 mrad. This FOV is well above the 0.1 mrad divergence of the laser and beam expander setup.

It is then necessary to verify that the angle of the signal exiting the convex lens to the fiber does not exceed the maximum entrance angle of the fiber. The numerical aperture of the fiber yields a maximum entrance angle of 19.88 degrees. Using trigonometry and the focal length of the convex lens, the diameter of the light at the convex lens would have to be greater than 11.42 mm to exceed the maximum entrance angle. Since the clear aperture of

the polarization splitting cube is 12 mm, the cube could be an aperture stop, but we will control the system aperture with a stop set at a well chosen location. Since the system will emphasize data above 1 kilometer, the 1 kilometer range will be the lower limit in calculating the diameter of the signal at the convex lens. Using the Gaussian lens formula

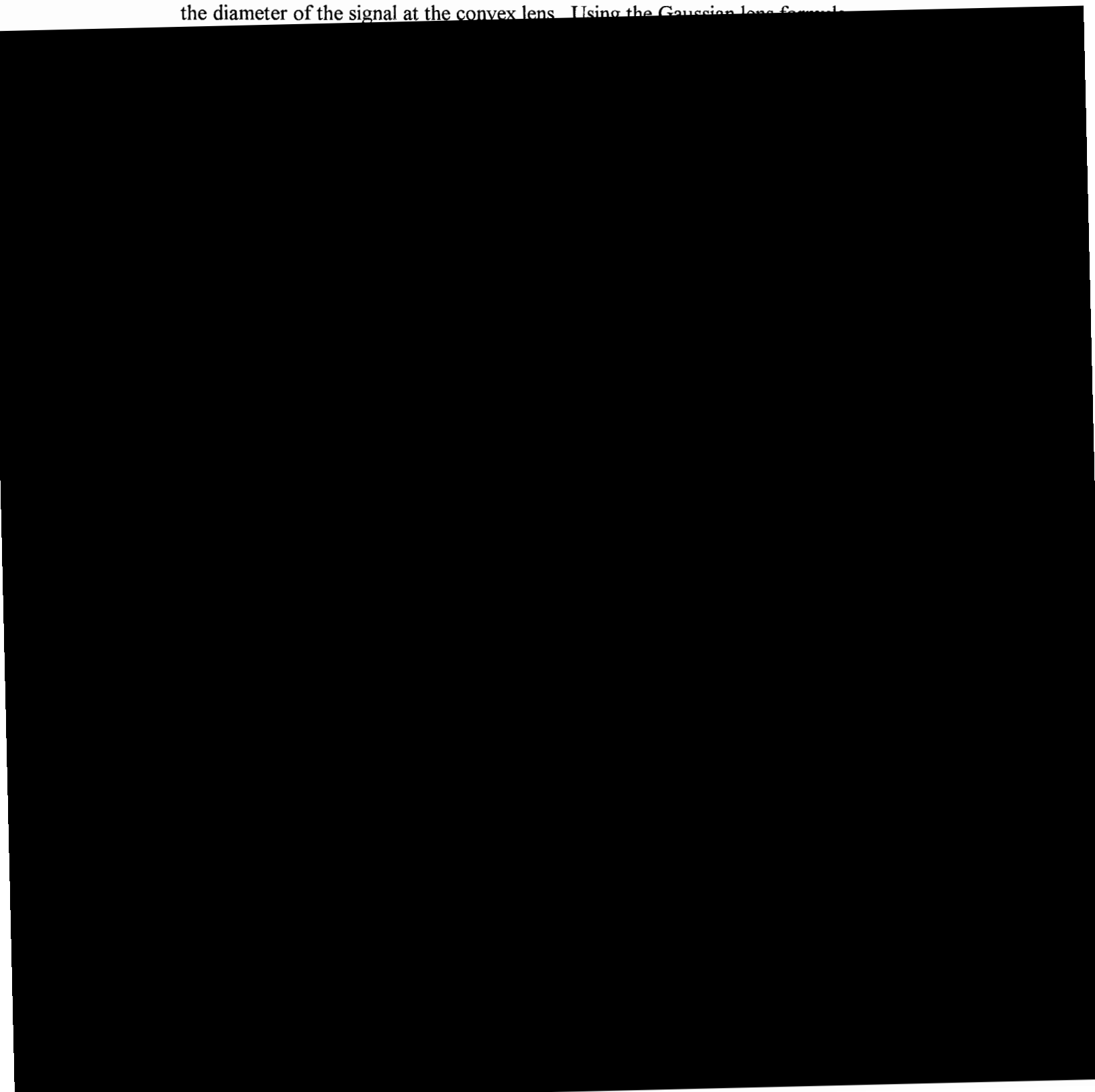

equation. This will cause the image distance, s_{ima}, of the telescope to move by 1 cm, for an altitude of 1 kilometer, compared to an infinity source. This may not seem like much, but results in the spot size at the fiber to overfill the fiber's core.

First, the telescopes image plane, IMT (s_{ima}), at an altitude, z (s_{obj}), is found using equation 3.4.,

$$\frac{1}{IMT} = \frac{1}{f_{tel}} - \frac{1}{z} \quad , \tag{3.6}$$

where f_{tel} is the telescope's focal length, equal to 3.17 m. At 1 kilometer, IMT equals 3.18 m.

This image plane distance is now used as the object distance for the concave lens. Because the negative lens' focal length (-60 mm) is always fixed to the telescope's infinity focal point, the total object distance is 0.060 + (IMT - f_{tel}) and the image point of the concave lens, IMC, is,

$$\frac{1}{IMC} = \frac{1}{f_{cc}} - \frac{-1}{0.060 + IMT - f_{tel}} \quad , \tag{3.7}$$

where f_{cc} is the focal length of the concave lens. The minus sign for the object distance in 3.7 is because the object distance is always behind the lens.

Next in the optical path is the polarization splitting cube which can be neglected. Therefore, the plano-convex lens is considered next. Again, the image distance of the concave lens, IMC, is used as the object distance for the convex lens, plus 4 cm are added due to the spacing between the two lenses (0.04 - IMC) and the equation is,

$$\frac{1}{IMX} = \frac{1}{f_{cx}} - \frac{1}{0.04 - IMC} \quad , \tag{3.8}$$

where IMX is the image distance of the convex lens and f_{cx} is the focal length of the convex lens (32.6 mm). This final equation will describe the location of the image point corresponding to the altitude range z.

To find the diameter of the spot at the fiber we use the magnification formula, 3.5, and trigonometry. This will require us to know the size of the laser beam at an altitude range, z. After expansion, the laser's exit diameter is 42 mm, and the laser's divergence is 0.1 mrad, therefore, the width of the beam at altitude z is,

(3.9)

Next, the beam width is multiplied by several magnification factors due to each optical element to determine the spot size at the final image point.

$$Spot\ size = Beam\ width \left(\frac{IMT}{z}\right) \left(\frac{IMC}{0.06 + IMT - f_{tel}}\right) \left(\frac{IMX}{0.04 - IMC}\right) \tag{3.10}$$

Now that the spot size has been calculated at the final image point, this image point may be in front, behind, or at the fiber entrance. Using simple trigonometry and angles, the spot size at the fiber entrance is calculated, and shown in Figure 3.4 for the detected wavelengths. Because of dispersion effects in the lenses, the altitude at which the telescope opens (all the return signal is coupled into the fiber) is different for each of the detected

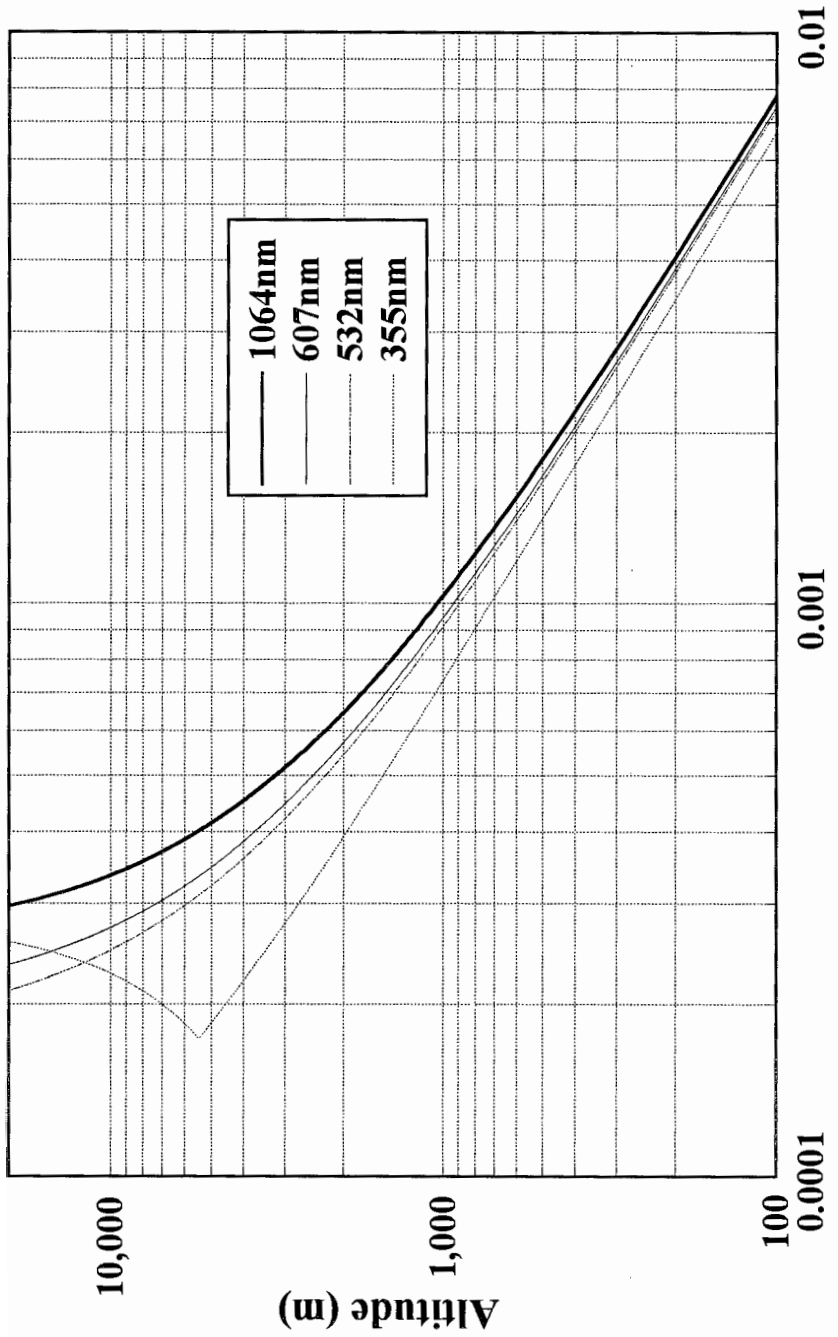

Figure 3.4. Diameter of the image spot at the front of the fiber

wavelengths.

In addition, the return signal from altitudes less than 1 kilometer is partially blocked by the telescope's secondary. The secondary, in effect, produces a dark image spot at the fiber core for the lower altitudes. In order to determine where the secondary does not play a significant role of blocking the lower altitude return signal, the secondary's diameter (6.75 inches) is now considered as if it was a separate telescope system. Equation 3.6 to 3.10 are again used, except the new telescope diameter is 6.75 inches to indicate where the blocking of the secondary will influence the system. Figure 3.5 shows the results of this procedure. As an example, for 1064 nm, Figure 3.5 shows that the return signal can start to be detected at 430 meters and then be fully detected at 1050 meters (Figure 3.4). Essentially below 430 meters, the secondary obstructs all of the return signal. In between these two distances, the percentage of the return signal detected is almost linear, starting at 0 percent at 430 m and being 100 percent at 1050 m. This assumes perfect alignment and no diffraction, whereas, in the actual system a return will most likely be obtained over the whole profile.

Finally, in order to setup the optics, the focal points of the telescope, concave lens and convex lens must be physically located. The telescope's focal point is found by looking at the moon (preferably a full moon) and moving a piece of paper until the craters on the moon can be sharply seen. The plano-convex lens' focal point is found by sending a collimated HeNe laser through the convex side and measuring the distance to the focal point from the plano side. The fiber is then set at this physical distance. The plano-concave lens' focal point is a little harder to find. Again, the collimated HeNe laser can be sent through the concave side, and by measuring the divergence a certain distance away and using angles the focal point can

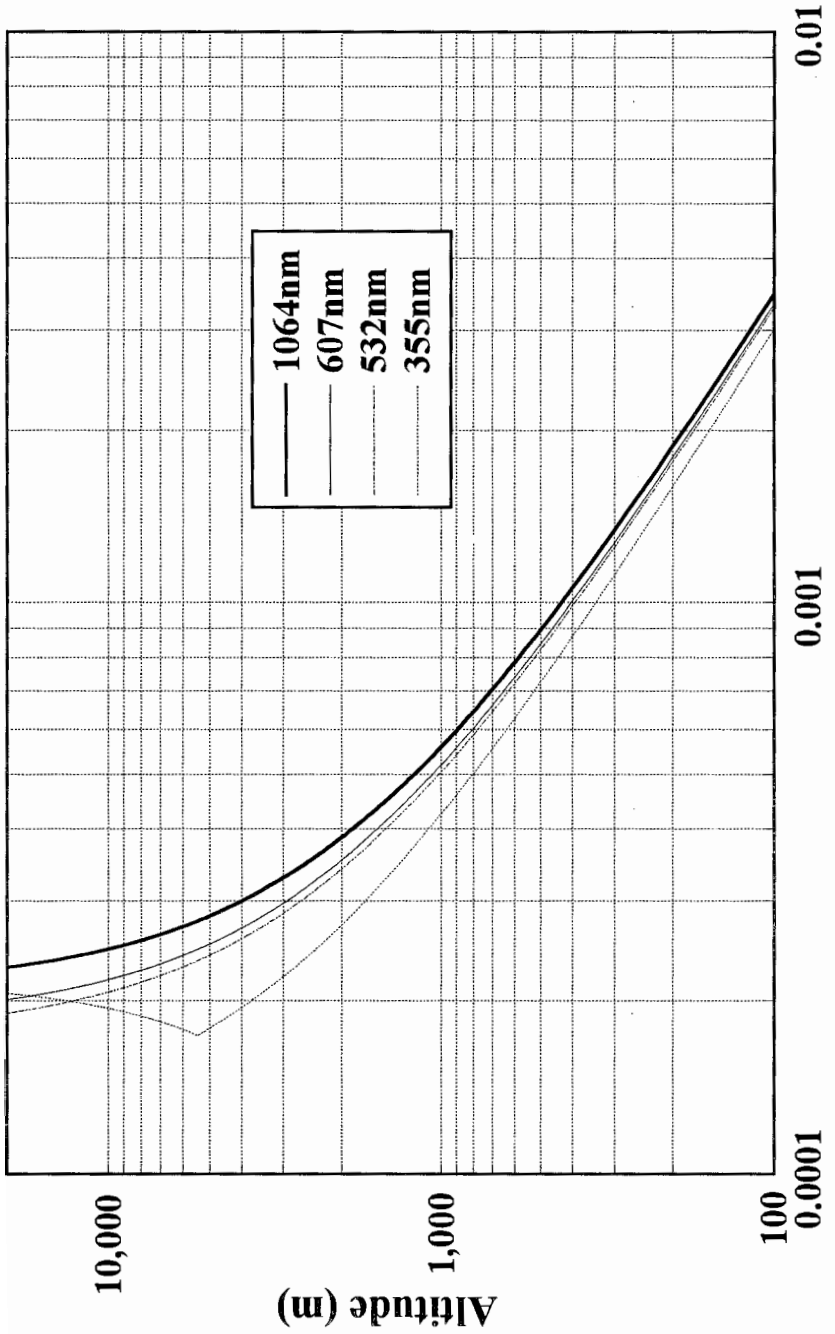

Figure 3.5. Diameter of the obstruction spot at the front of the fiber due to the telescope's secondary

be found. When setting up the combination concave lens and telescope in the polarization divider box correctly, collimated light should be observed when looking at a distant object, such as the moon (the craters on the moon should be clear). This method was tried, and craters on the moon were clearly observed.

3.5 Optical Fibers

An optical fiber is used to transfer each of the polarization components (S or P) from the polarization divider box to the detector box. The optical fiber chosen has a 1 mm diameter fused silica core, with a stainless steel monocoil outer shell. The trade-off on the fiber's core diameter includes the following factors: at large core diameters, the FOV of the telescope is greater resulting in more background, the altitude at which the laser is entirely in the FOV is lower, and the fiber is more likely to be broken because of its larger value of a minimum bend radius. The 1 mm diameter has already been used in LAMP and has proven reliable. According to the manufacturer, Fiberguide Industries, the long term minimum bend radius of the 1mm fiber is 11.81 inches and the momentary (minutes) minimum bend radius is 3.94 inches. The fused silica core was selected because it provides better transmission at 355 nm than glass or plastic cores. Finally, because the fibers will be susceptible to being stepped on when out in the weather and laying on the ground, a stainless steel monocoil was added to the outside of the fiber to lower the possibility of damage.

The fiber's numerical aperture (NA) has previously been stated as equal to 0.34. This is not exactly the case, as the fiber's NA is wavelength and length dependent. According to the manufacturer's data, for fiber lengths over 50 meters the NA is approximately 0.23. For

a fiber length of 2 meters, the NA is 0.40. From 2 meters to 50 meters, the NA is almost a straight line (curve provided by manufacturer). For a length of 10 meters, the curve indicates the NA is approximately 0.34. In addition, the NA versus wavelength curve was provided by the manufacturer for a 5 meter length. For the 1064, 607, 532, and 355 wavelengths the NA is 0.388, 0.391, 0.389, and 0.382, respectively. From the numerical apertures given versus wavelength, there is only a maximum difference of 2.3 percent, therefore, 0.34 has been used for all calculations. The index of refraction has been calculated (equation provided by manufacturer) and is 1.4496, 1.4578, 1.4607, and 1.4761 for 1064, 607, 532, and 355 nm, respectively.

The LARS lidar sits outside of its container and is connected with the computers, laser, and detector box through an umbilical cord containing data lines, power lines and the optical fiber. This cord will be twisted, bent, moved in different positions since LARS is a rotating system. The fiber must be protected from bending and any extra fiber should be coiled in the container. Questions have arisen as to what is the loss or if there is a loss of signal due to this curvature and if entrance angle will play a role in the loss. An experiment was devised to test for curvature loss.

This experiment consisted of coupling a CW HeNe laser into the fiber and measuring the fiber's output while the fiber is being bent at different radii of curvature. First, the HeNe is expanded and collimated and sent through three different apertures. The different apertures were used to produce different entrance angles of the HeNe laser beam into the fiber, slightly above, slightly below, and half the maximum entrance angle. After the aperture, the collimated light was sent through a plano-convex lens, the same lens used in the polarization

splitter box, and into the fiber. The fiber was located at the focal point of the lens. The other end of the fiber was placed in front of a power meter. The active area of the power meter is large enough to capture all of the fiber's light. The fiber is then curved to different radii of curvature, down to the long term minimum bend radius of 11.81 inches (12 inches) to check for loss and compared to the energy reading when the fiber is totally straight. In addition, the different apertures are used with each different radius of curvature to simulate the different entrance angles. The results of the test showed that even down to the long term minimum bend radius, no optical losses were observed in the fiber.

3.6 Receiver Optical Efficiency

Examining the lidar equation (1.2), one of the factors the return signal is dependent on is the receiver efficiency. If in a certain range, 200 photons are collected by the telescope, and the receiver subsystem is 10 percent efficient, only 20 photons will be measured at the detector box. Knowing the receiver optical efficiency is therefore important to determine if the actual data will be similar to the modeled data.

All three areas, the telescope, the polarization divider box, and the fiber, are prone to losses. The telescope loss is due to the coatings on the mirrors. The mirrors are coated with flashed aluminum with an SiO_2 overcoat and have a different reflectance at each wavelength. A witness sample of the coating was not obtained during purchase, so Optical Guidance Corporation quoted a worst case reflectance for each wavelength for a mirror. Since the telescope has two mirrors, the total telescope efficiency will be the reflectance squared (summation in Table 3.1).

The polarization divider box contains three uncoated lenses, the polarization splitter cube, and the optical fiber. The lenses and the polarization cube were measured in the spectrophotometer (results in Table 3.1). One difficulty which was encountered when measuring the polarization splitting cube, was due to the fact the S polarization is split off at an angle and could not be measured. Since both the input and output interface is at normal incidence to the S polarization, the Fresnel coefficients were used and multiplied by the transmission of calcite, in order to determine the cube's transmission.

To determine the loss due to the fiber ends, the Fresnel coefficients were employed for each polarization using an entrance angle equal to the maximum entrance angle of the fiber. To determine the attenuation of the fiber, the manufacturer provided a transmission curve versus wavelength for the fiber (summarized in Table 3.1).

Table 3.1. Receiver optical efficiency

Wavelength	1064 nm	607 nm	532 nm	355 nm
Telescope	0.92	0.88	0.89	0.90
Plano convex lens	0.940	0.940	0.938	0.932
Plano concave lens	0.937	0.935	0.934	0.920
Polarization splitting cube				
P polarization	0.888	0.880	0.874	0.556
S polarization	0.858	0.857	0.854	0.523
Fiber ends				
P polarization	0.936	0.935	0.934	0.930
S polarization	0.931	0.929	0.928	0.924
Fiber transmission (10 m)	0.955	0.970	0.959	0.737
Total efficiency				
P polarization	0.643	0.617	0.610	0.294
S polarization	0.618	0.597	0.593	0.275

Chapter 4

Conclusion

The preceding two chapters are essential in understanding the components of the lidar transmitter and receiver and will provide useful insight in interpreting the data or correcting problems with the system. Preliminary data has been taken with the LARS lidar and is shown in Figures 4.1 and 4.2. Figure 4.1 displays a 1 second data run, average of 20 laser pulses, 7.5 meter resolution, for the 532 nm channel. This one second average will be employed when the system is scanning. Several cloud layers are seen up to 2 kilometers, and another cloud layer around 7 kilometers. The lower altitude maximum return, where the telescope opens, is around 600 meters, indicating that the polarization divider box is not yet correctly aligned (Figure 3.4). This can also be deduced from the fact that the signal drops off sharply after 2 kilometers.

Figure 4.2 presents a 10 minute data run, for the 532, showing several cloud layers up to 7 kilometers. This extended time of averaging will be employed if the system is stationary. The telescope again opens at 600 meters and the signal drops off sharply in between cloud layers.

4.1 Future Work

As always, there is more work that can be done on the system to improve and understand the performance at the time of the first data acquisition run. The initial results shown here are the first steps of testing and evaluation of the system which will take place during the next several months. This section will discuss several areas where future efforts

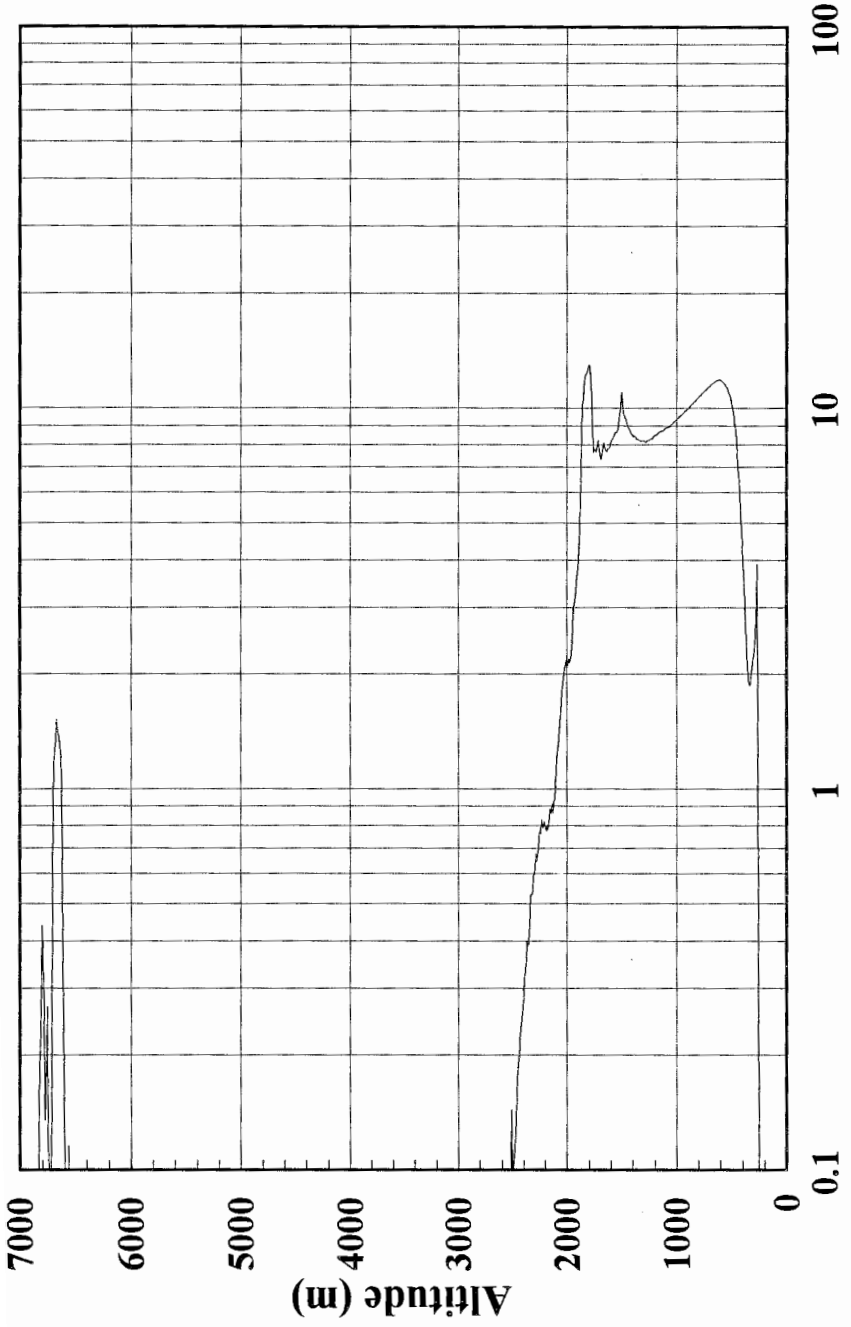

Figure 4.1. 532 nm backscatter return for a 1 second data run showing several cloud layers (November 3, 1994)

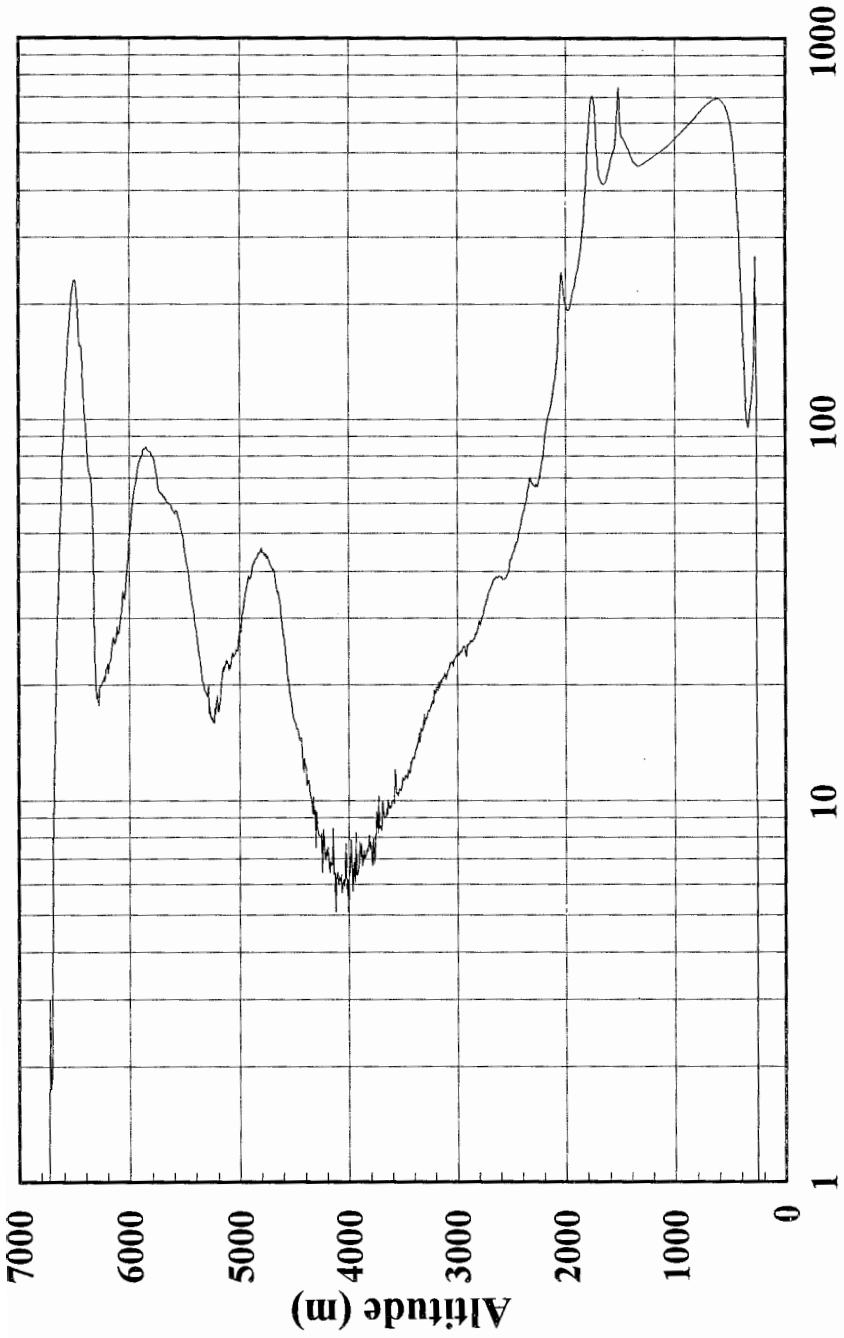

Figure 4.2. 532 nm backscatter return for a 10 minute data run showing several cloud layers (November 3, 1994)

can improve the instrument. It is anticipated that several upgrades and improvements will be implemented during the next year.

First, the laser's 532 crystal should be replaced with a type I crystal, because the type II crystal changes the output of the 1064 to an elliptical polarization and reduces the 355 nm energy by 25 percent. The motorized mirror mount, MM1, should be incorporated into a computer controlled program which would align the laser in the field of view of the telescope automatically by maximizing the signal return at an altitude between 1 and 5 kilometers. Since the LARS system is used in the cold weather, it would be useful to still pursue finding an anti-freeze solution for the laser head cooling. The energy monitor could be duplicated and placed behind each of the two inch hard coated mirrors. This set-up could indicate when the mirrors are burned and need to be rotated. Also, the data from the energy monitor should be incorporated into the data acquisition system to record the average energy over a 1 second data run. The hard coated mirrors should be recoated with a higher reflectance for the 355 wavelength, because of the low reflectance with the present mirrors. The polarization of the final output signal needs to be determined. This can be accomplished by obtaining another Glan-Thompson polarizer and testing each wavelength off a 45 degree mirror. In addition, sampling part of the final exiting expanded beam (since the beam expander may cause a depolarization) should be used to verify the polarization characteristics of the combined elements.

The polarization splitter box's optics should be AR coated for the visible, to reduce the reflectance losses. The coating should be a single MgFl coating, because this coating will not cause there to be more than the normal Fresnel losses at 355 nm and 1064 nm. The

polarization splitter box needs to be correctly aligned, and optical mounts be machined so that the optical elements can be removed and then returned exactly to their original position.

References

Continuum, *Operation and Maintenance Manual Surelite II*, California, 1992.

E&G Judson, *Silicon Photodiodes*, Massachusetts, 1990.

Fiberguide Industries, *Optical Fiber Products*, New Jersey, 1991.

Rudolf Kingslake, *Optical System Design*. Orlando: Academic Press, Inc., 1983.

R. M. Measures, *Laser Remote Sensing*. Florida: Krieger Publishing Co., 1992.

K. Sassen, "The Polarization Lidar Technique for Cloud Research: A Review and Current Assessment," Bull. of the Amer. Meteo. Soc., vol. 72, no. 12, 1848-1866, 1991.